國立臺灣大學工學院工程科學與海洋工程學系

碩士論文

Department of Engineering Science and Ocean Engineering

College of Engineering

National Taiwan University

Master Thesis

加重塊在淺水海域極限環境條件下對2兆瓦浮動式離岸風力發電機繫泊系統的影響

Influence of Clump Weight on 2 MW Floating Offshore Wind Turbine Mooring System in Extreme Sea Condition and Shallow Water

五十嵐雪姬

IGARASHI YUKI

指導教授：馬開東 博士

Advisor : Kai-Tung Ma Ph.D

中華民國 112 年 7 月

July 2023

doi:10.6342/NTU202303528

致謝

轉眼間來台灣已經五年了。五年前隻身來台灣的我從未想過我會成為現在的自己。這篇論文是我作為台大學生的一個終點，但同時也是我人生新的篇章的起點。在這段旅途中最感謝的是謝文紀學長在我最迷茫的時候為我指了一條路，讓我有堅持的勇氣。也無比感謝丁肇隆教授不止當了我大學三年的導師，也一直從旁提點一路磕磕絆絆的我，更成為了最讓我安心的存在。

本論文能順利完成要特別感謝馬開東指導教授的支持。兩年的研究生生活裡，馬老師提供了一個充滿學習機會的環境，也讓我在跌跌撞撞中找到了自己想走的路。另外也要特別感謝陳東輝顧問在我每次想不出癥結點的時候提點我，讓我發現自身視角的盲點，並細心的跟我解釋。每次找陳顧問詢問問題的時候都讓我有更多新的思路、新的想法，總讓我感嘆自身還有太多太多需要繼續學習的地方卻也讓我對未知的部分充滿好奇。除此之外也要感謝吳哲芳顧問對我不管是學業上還是待人處事上的諄諄教誨，是我們實驗室當之無愧最溫柔的後盾。

這篇論文能順利產出也要感謝實驗室裏的每一位成員。因為有你們的存在，我研究生的生涯裡一直都不是孤軍奮戰。不管是一仁、宏駿、在天、昭瑜還是已經從我們實驗室畢業的其昂和愷鴻，真的很感謝你們出現在我的人生裡。雖然總是打打鬧鬧，但你們讓本該煩悶的生活裡多了許多色彩和牽絆。對於我們實驗室我只想說，我們實驗室真的不能沒有徐一仁！！！除了感謝真的不知道還能說什麼。希望未來的大家都能一帆風順，都能成為理想中的自己。特別要注明一下本論文使用的浮台是雲在天同學通過參數分析設計出來的臺大浮台的縮小版。

除了實驗室以外也要感謝船舶中心專案組的大家。感謝政彰學長和彥威學長每次在我遇到相關問題的時候都會迅速幫我解答，也要感謝鍾博總是很樂於給我們這些學弟妹們機會。

接下來要重點感謝一直陪伴在我身邊的宗霖和嘉晴，沒有你們的生活我真的無法想象。也感謝我這學期的室友藝瀟，有你在的宿舍讓我每天都有回家的感覺。感謝我們黨的小朋友們讓我在碩二還能當個小朋友。尤其是Ryan還在我口試前一天在幫我順稿。最後的最後要感謝我的媽媽不管我做什麼決定都支持我，也感謝我的姐姐總是對我無比的寬容以及無私的付出。

一切都將會越來越好的！

doi:10.6342/NTU202303528

Abstract

This study aims to investigate the influence of the clump weight on a 2 MW floating offshore wind turbine (FOWT) mooring system, focusing on extreme sea conditions and shallow water effects. This study primarily focuses on the extreme values of the 6 degrees of freedom (6 DoF) and the maximum line tension of the mooring lines to assess the impact of clump weights on the mooring system. Three parameters related to the clump weight were studied, including the starting position of clump weights, spacing between clump weights, and the number of clump weights. The objective was to evaluate the performance differences resulting from these parameters on the effectiveness of the clump weights. The findings indicate that selecting a starting position for the clump weights located after the touchdown point has relatively better performance. When the spacing between clump weights is too small, in this case, 2 meters and 3 meters, localized extreme line tension may occur. Due to the fact that clump weights will all be lifted from the seabed under extreme environmental conditions, the more clump weights there are, the greater the maximum tension along mooring lines. The possible reason for this outcome may primarily lie in the total weight of the clump weights. In the case of shallow water, the inclusion of clump weights in the system does not consistently improve the overall performance compared to the system without clump weights in shallow water regions with extreme sea state. This study suggests the need for further research to explore the feasibility and potential advantages of using clump weights to optimize mooring systems in shallow water environments.

Keywords: Floating Offshore Wind Turbines, FOWTs, Mooring System, Clump Weight, Extreme Sea Conditions, Shallow Water

doi:10.6342/NTU202303528

摘要

本研究旨在探究加重塊在極端海況和淺水環境中對2兆瓦浮動式離岸風力發電機繫泊系統的影響。研究主要關注浮台六個自由度的極限值以及錨鏈的最大張力以探討加重塊對於繫泊系統的影響, 包含了加重塊相關的三個參數。分別爲加重塊的起始位置、加重塊的間距以及加重塊的數量。分析的目的是評估這些參數的改變如何影響繫泊系統的性能。研究結果顯示，將加重塊起始位置設定於著陸點之後的地方具有相對較好的性能。當加重塊之間的間距過小，以本研究爲例爲2米和3米時，錨鏈會出現局部極端的張力。由於加重塊在極端環境條件下會被全部被拉起，離開海床，因此加重塊越多，錨鏈的最大張力越大，而造成此結果的原因可能主要來自加重塊總重量的差異。通過針對參數的探討，發現加入加重塊後的系統在淺水海域極限條件的情況下并沒有優化繫泊系統的性能。因此本研究建議進行進一步的研究，以探索在淺水環境中使用加重塊來優化繫泊系統的可行性和潛在優勢。

關鍵詞：浮動式離岸風力發電機、繫泊系統、加重塊、極端海況、淺水海域

doi:10.6342/NTU202303528

Nomenclature

Latin Symbol

a	Acceleration	$[m/s^2]$
a_b	Body acceleration rel;ative to earth	$[m/s^2]$
a_f	Fluid acceleration relative to earth	$[m/s^2]$
a_i	Internal stress area	$[m^2]$
a_{r}	Relative fluid acceleration	$[m/s^2]$
a_o	External stress area	$[m^2]$
A	Drag area	$[m^2]$
AM	Added mass contribution to clump inertia	$[te]$
c	Damping coefficient in seconds	[-]
c_c	Critical Damping	[-]
C_a	Added mass coefficient	[-]
C_d	Drag coefficient	[-]
C_i	Centroid	$[m]$
C_m	Inertia coefficient	[-]
D	Draught	$[m]$
EA	Axial stiffness	$[kN/m]$
f_A	Drag load	$[kN/m]$
f_c	Cyclic frequency	$[1/s]$
f_D	Additional mass load	$[kN/m]$
f_m	Peak frequency	$[1/s]$
f_M	Fluid force per unit length	$[kN/m]$
g	Acceleration due to gravity	$[m/s^2]$

doi:10.6342/NTU202303528

G	Green's theorem	[-]
h	Water depth	$[m]$
J_0	Beseel function	[-]
k	Wave number	[-]
K	Stiffness	$[kN]$
l	Instantaneous length	$[m]$
l_0	Unstretched length	$[m]$
L	Length between perpendicular	$[m]$
L_K	Integral scale parameter	[-]
m	System mass	$[te]$
m_A	Added mass	$[te]$
m_z	Yaw moment	$[kN/m^2]$
p	Position	[-]
p_i	Internal pressure	$[Pa\ ]$
p_o	External pressure	$[Pa\ ]$
P_i	Pressure at i^{th} panel	[-]
$q_B^{\pm}$	Force function	[-]
$q_F^{\pm}$	Force function	[-]
s_z	Axial direction	[-]
S	Current speed	$[m/s\ ]$
S_f	Current speed at the surface water	$[m/s\ ]$
S_b	Current speed at the seabed	$[m/s\ ]$
t	Simulation time	$[s\ ]$
T_e	Effective tension	$[kN\ ]$
T_w	Wall tension	$[kN\ ]$
U	Velocity of moving body	$[m/s\ ]$

doi:10.6342/NTU202303528

v	System velocity	$[m/s\ ]$
v_{r}	Relative fluid velocity	$[m/s\ ]$
V	Wind speed	$[m/s\ ]$
z_r	Data height	$[m]$

Greek Symbol

α	Complex displacement RAOs for rotation	$[rad/m]$
β	Wave heading	[°]
ϵ	Total mean axial strain	[-]
ξ	Complex displacement RAOs for translation	[°]
γ	Peak enhancement factor	$[m/m]$
ρ	Density	$[te/m^3]$
$\bigtriangledown \mathbf{\Phi}$	Gradient of velocity potential	$[m/s^2]$
$\mathbf{\Phi}$	Velocity potential	$[m^2/s]$
$\phi^{(1)}$	First-order complex potential	$[m^2/s]$
$\phi_I^{(1)}$	Potential of the incident wave	$[m^2/s]$
$\phi_R^{(1)}$	Radiation potential	$[m^2/s]$
$\phi_S^{(1)}$	Scattered potential	$[m^2/s]$
$\phi^{\pm}$	Second-order complex potential	$[m^2/s]$
$\phi_I^{\pm}$	Second-order potential in the absence of the body	$[m^2/s]$
$\phi_R^{\pm}$	Second-order radiation potential	$[m^2/s]$
$\phi_S^{\pm}$	Remainder of $\phi^{\pm}$	$[m^2/s]$
ω	Angular frequency of wave	$[rad/s]$
ω_i	Frequencies of incident waves	$[1/s]$

doi:10.6342/NTU202303528

ω_j	Frequencies of incident waves	$[1/s]$
ω_y	Yawing rate	$[rad/s]$
Ω	Angular velocity	$[rad/s]$
ν	Poisson ratio	[-]
τ	Segment twist angle	$[rad]$
$\triangle$	Mass of fluid displaced	$[te]$

doi:10.6342/NTU202303528

Content

doi:10.6342/NTU202303528

doi:10.6342/NTU202303528

List of Figures

doi:10.6342/NTU202303528

List of Tables

doi:10.6342/NTU202303528

doi:10.6342/NTU202303528

Chapter 1

Introduction

1.1 Background

Many countries have made commitments to reach net-zero emissions by 2050 or earlier, recognizing the importance of transitioning to a low-carbon economy to mitigate the impacts of climate change. The Paris Agreement [1], signed in 2015, serves as a key global framework for addressing climate change, with the long-term goal of limiting global warming to well below 2°C above pre-industrial levels and striving to keep it below 1.5°C. As energy-related carbon dioxide (CO_2) emissions represent two-thirds of all greenhouse gasses [2], energy transition from fossil fuel to renewable energy is imminent.

Taiwan, a small island with its abundant coastal resources and favorable wind conditions [3][4], has emerged as a frontrunner in offshore wind development in the Asia-Pacific region. In 2017, the Taiwanese government had set an ambitious target of generating 20 % of electricity from renewable sources by 2025 including 5.7 GW of offshore wind power [5]. Several strategies have been implemented to promote offshore wind power, including carrying out the world's highest feed-in tariff (FIT) [6] for renewable energy to attract foreign investment and a Four-year Wind Power Promotion Plan [7][8]. Additionally, a Local Content Requirement (LCR) policy has been implemented by the government to promote the development of a local supply chain for offshore wind power projects [9][10].

In 2012, Taiwanese government announced “Offshore Wind Power System Demonstration Incentive Regulations”, which under the first of the 3 phases strategies

doi:10.6342/NTU202303528

[10] for offshore wind, to award grants to four to six demonstration offshore wind turbines scheduled for completion in 2015 [8] to increase confidence of developers and encourage development of offshore wind. The second phase of the strategies for offshore wind is Zone Application for Planning. Bureau of Energy, Ministry of Economic Affairs, R.O.C. announced 36 Zones of Potential along Taiwan's coastline near Changhua and Miaoli that have been identified as suitable for offshore wind farm development and aimed to attract more investment and promote the growth of the offshore wind industry in Taiwan [5].

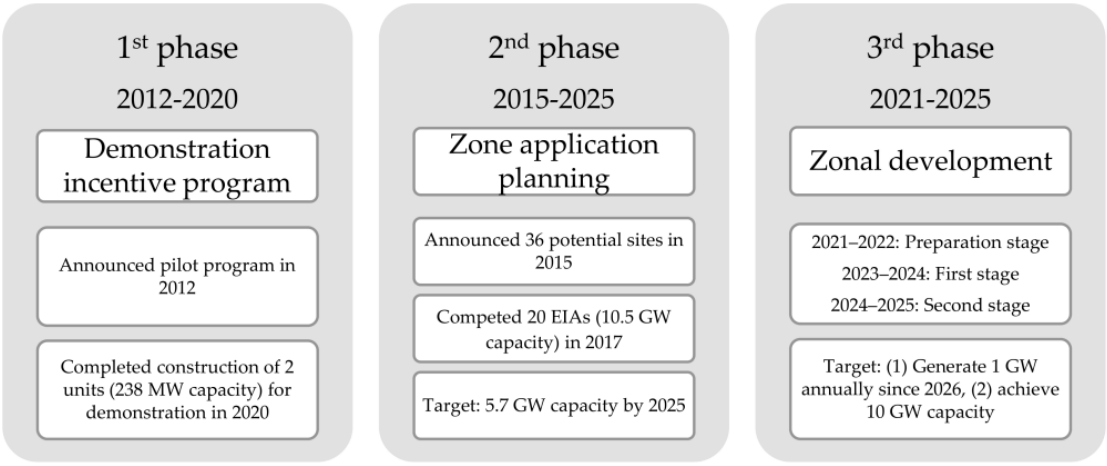

Figure 1. The three phases of Taiwan's offshore wind energy policy [10]

Building upon the success of Phase 1, which is the completion of the first offshore wind farm in Taiwan, Taiwanese government announced Phase 3 Offshore Wind Zonal Development in August 2021. Total 15 GW of capacity is planned to be released during 2026 to 2035 [12]. As Figure 2. [13], wind power capacity is expected to be much higher in deeper regions, thus, developers targeted deeper water regions. From the publicly available data from developers [14][15][16], water depth of selected projects had come up to 96 m.

doi:10.6342/NTU202303528

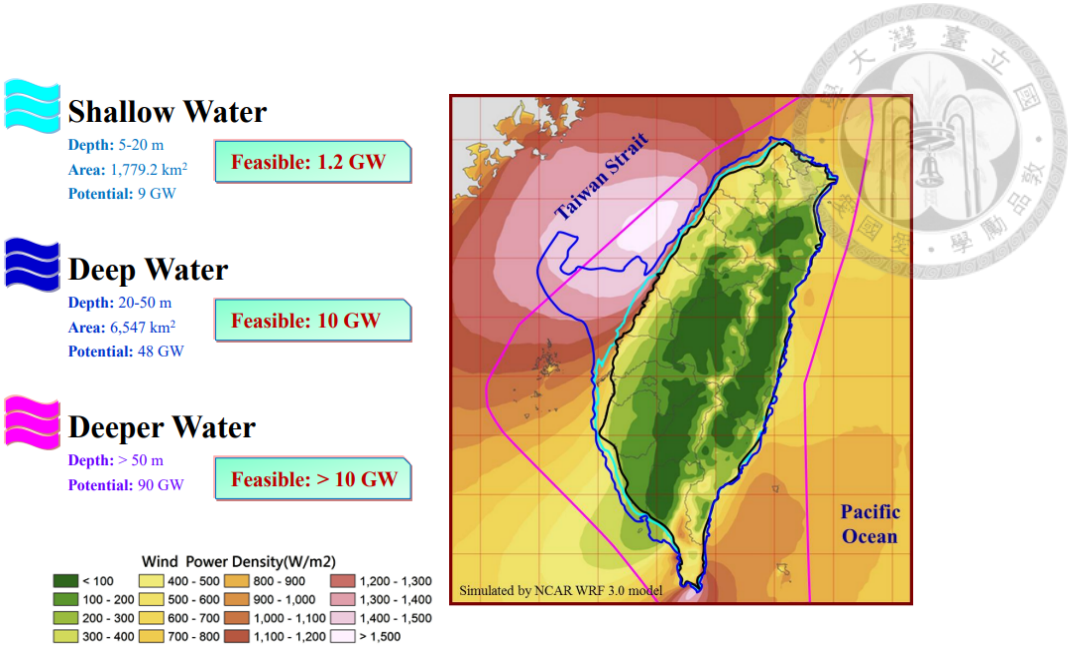

Figure 2. Taiwan offshore wind potential [10]

Up till Phase 2 , as water depth mostly not more than 50 m, only fixed bottom type foundation such as monopile and jacket type is used. Previous research showed that the cost of fixed bottom type foundation will become relatively high to achieve the required stability [17][18]. Thus, discussion about floating offshore wind turbines (FOWT) trending straight up.

doi:10.6342/NTU202303528

1.2 Literature Review

The concept of large scale floating offshore wind turbines might be tracked back till the early 1970s, Professor William E. Heronemus surmised they would be large windmill-like structures that made power on land or on platforms floating in the ocean in the future [19]. But only until the 1990s, after wind power started commercialization, the topic was taken back to research. In 1993, K.Tong and C. Cannell had studied the feasibility of using floating platforms for wind turbines [20], while N. Barltrop had listed the pros and cons of floating offshore wind farms and proposed a V shape floating wind farm shown in Figure 3. [21]. Meanwhile, A model test for a moored platform for wind turbines designed for water depth 20 m to 100 m is derived almost at the same time [22].

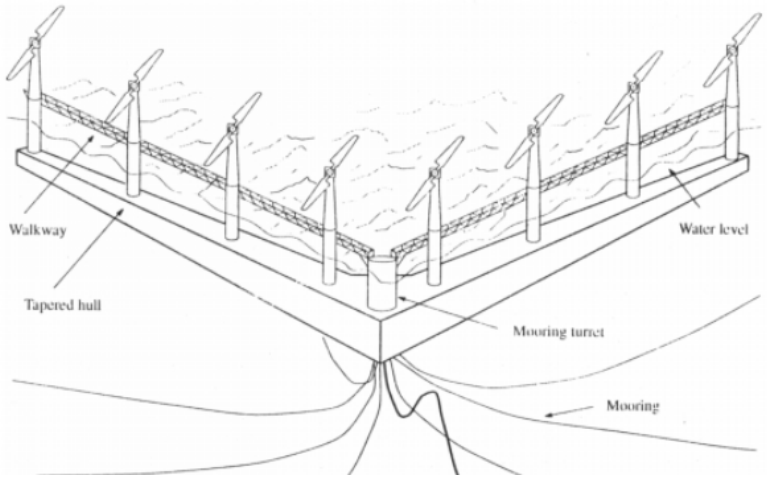

Figure 3. Multiple unit offshore wind farm [20]

Unlike fixed-bottom offshore wind turbines, floating wind turbines are mounted on floating platforms or foundations. Generally, floating platforms could be classified into four types which are semi-submersible, spar, tension leg platform and barge type floating platform as shown in Figure 4. [23]. The categorization of these platforms are

doi:10.6342/NTU202303528

dependent on the method of achieving static stability such as shown in Figure 5. [24][25]. Each of these stability approaches can be conceptualized as an idealized vessel with specific characteristics while the designer seeks the satisfactory balance.

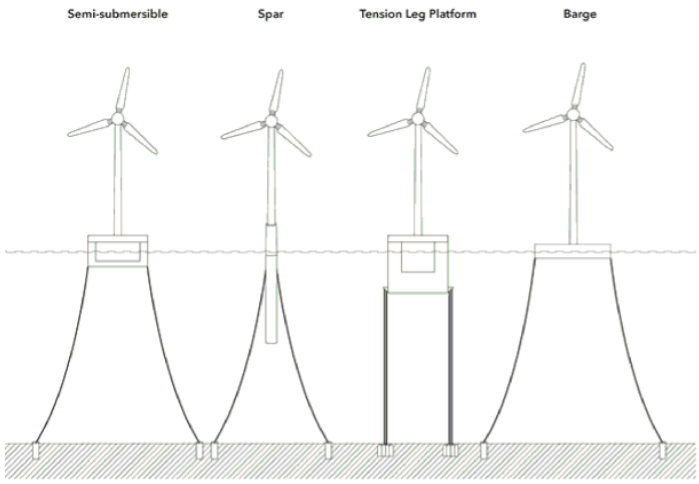

Figure 4. Types of floating platform [20]

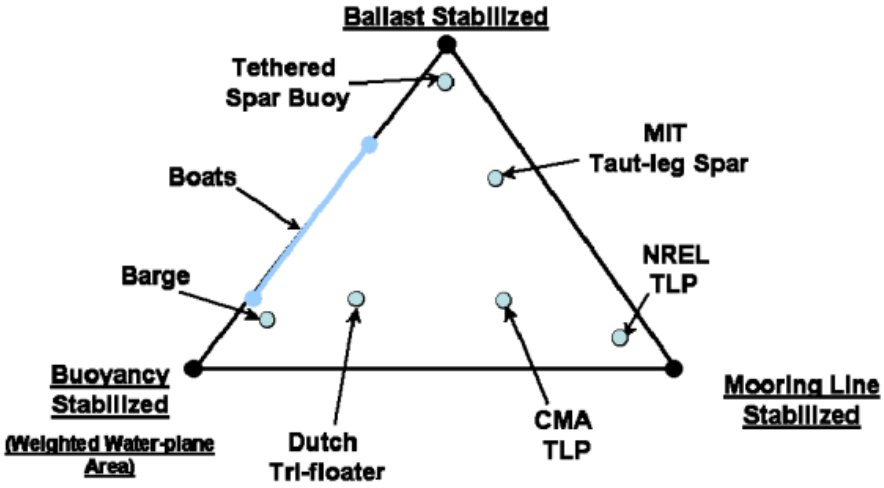

Figure 5. Floating platform stability triangle [25]

Based on these concepts, plenty of research has been done. W. Musial et al. [26] offers a comprehensive technical overview of various floating platforms designed for wind turbines. S. Bashetty et al.[27] compared the dynamic motion of TLP type, spar type, and semi submersible type FOWT. I.J. Hsu et al. [28] optimized a

doi:10.6342/NTU202303528

semi-submersible FOWT system based on Taiwan environment conditions, G. Ferri et al. [29] enhanced a 10 MW FOWT system.

Beside a floating platform, a tailored mooring system is essential for a FOWT to protect the dynamic cable and address risks such as earthquakes or typhoons. Different types of mooring systems are employed based on specific requirements and environmental conditions. There are three commonly used mooring system types for FOWTs which are catenary, semi-taut, and taut mooring systems [30].

Catenary mooring involves the attachment of multiple mooring lines to anchor points on the seabed, forming a natural curved catenary shape based on the combination of their weight and the platform's tension. This configuration is predominantly employed in shallower waters and under moderate environmental conditions. In a semi-taut mooring system, the mooring lines exhibit a slight sag while retaining a certain level of tension, striking a delicate equilibrium between the flexibility of a catenary system and the heightened stability provided by taut mooring. Taut mooring systems, on the other hand, maintain constant tension in the mooring lines, minimizing platform movement and ensuring enhanced stability. Such a system effectively restricts the platform's motion to a confined area, facilitating superior control and maneuverability [31].

As expense is a critical factor of developing FOWT, an effective mooring system is desired. A. Neisi [32] proposes a new multi-segment arrangement. M.J. Harrold [33] studied the effect of a hydraulic mooring component with non-linear stiffness in the FOWT mooring system. G. Barbanti [34] states that attachment of clump weight on mooring lines may improve FOWT response and lower fatigue damage.

doi:10.6342/NTU202303528

1.3 Motivation

Under encouragement of localization, National Taiwan University (NTU) jointly with Ship and Ocean Industries R&D Center (SOIC) and China Shipbuilding Corporation Taiwan (CSBC) designed a floating platform named “TaidaFloat” [28] and plan to manufacture a 2 MW prototype FOWT in Taiwan Strait. Taiwan Strait, with an average water depth of 60m faces three to four typhoons annually [35] making harsh environmental conditions for FOWT to develop. Considering that a 2 MW may be important as the first step to develop FOWT in Taiwan, a 2MW semi-submersible platform is considered in this study.

Taiwan Strait is not more than 100 m deep. According to considerations in the offshore oil and gas industry, water can be deemed shallow when its depth is below 200 meters [36]. The main effect of shallow water to the mooring system is limitation of the catenary shape of mooring system and surface waves affect the water flow on the seabed.

In shallow water, the mooring lines have less freedom to form a natural catenary profile due to the limited water depth. This can result in increased line stiffness and reduced dynamic response, making the mooring system more susceptible to sudden loads and movements.

Water waves are surface waves, known as 'Rayleigh waves', a mixture of longitudinal and transverse waves. In the case of shallow water waves, water molecules follow oval orbits, and as one moves further from the surface, the diameter of the orbit decreases. This motion remains significant up to a distance of about one wavelength.

A 3x3 mooring system with 10 clump weights attached in each mooring line is designed for a 15 MW FOWT in Taiwan Strait [37]. The cost of mooring lines and its installation fees might become extremely high due to the massive mooring system. N.

doi:10.6342/NTU202303528

Bruschi [38] studied a few parameters of clump weight based on Hywind OC3 spar type FOWT in 320 m water depth which show positive influence in surge motion.

Addition of clump weight could provide stability to the floating platform by counteracting buoyancy and helps maintain the desired position and orientation of the structure against environmental forces. Clump weight also aids in controlling the tension of the mooring lines, ensuring optimal stiffness and response of the system. Furthermore, it contributes to the dynamic response by damping the motion induced by waves, improving overall stability and reducing fatigue loads [31].

N. Bruschi [38] indicates that selecting a lighter weight and placing it as closer to the platform would optimize the platform's response while minimizing the rise in fairlead tension while C.A. Chen [37] states that clump weight should position after the touchdown point. Therefore, clump weight starting position is chosen to be one of the variables.

The number of clump weights may influence the total cost to develop FOWT. Greater number of clump weights might result in higher costs related to manufacturing, installation and inspection. Moreover, transportation and handling expenses may escalate as well, especially facing shortage of available working vessels. In this case, optimizing the mooring system with lesser clump weight is worth studying. Thus clump weights spacing and number of clump weights is considered as our parameters.

doi:10.6342/NTU202303528

1.4 Structure of Report

- Chapter 1 provided an overview of the study, including its background, literature review, and motivation.
- Chapter 2 outlined the rules and regulations, design load case, design basis, and the simulation software utilized.
- Chapter 3 detailed the numerical methods employed throughout the research.
- Chapter 4 introduced the fundamental model setup adopted for the study.
- Chapter 5 analyzed the control case.
- Chapter 6 described the case settings for parametric studies of clump weight, presented the simulation results, and conducted discussions.
- Chapter 7 served as the conclusion for this thesis.

doi:10.6342/NTU202303528

Chapter 2

Design Criteria

2.1 Rules and Regulations

Compliance with rules and regulations for FOWT is crucial for ensuring the secure, dependable, and eco-conscious advancement, construction, and operation of a project. Rules and regulations additionally have a part in acquiring insurance coverage and financing for FOWT projects, as numerous insurance companies and financing institutions necessitate adherence as a prerequisite. The ensuing thesis takes into account the following set of rules and regulations:

- ABS, Guidance Notes on Global Performance Analysis for Floating Offshore Wind Turbines 2020 [39]
- ABS, Guide for Building and Classing Floating Offshore Wind Turbines 2020 [40]
- IEC 61400-3-2: 2019, Wind energy generation systems – Part 3-2: Design requirements for floating offshore wind turbines [41]

doi:10.6342/NTU202303528

2.2 Design Load Case

According to ABS, Guide for Building and Classing Floating Offshore Wind Turbines 2020, the design load conditions (DLC) and serviceability load conditions (SLC) are utilized to represent the design requirements for FOWT. The guide lists a total of 10 turbine conditions and 35 design load cases. To maintain the integrity of the mooring system for FOWT, it is essential to meet all the specified DLCs as a minimum requirement. Moreover, it is crucial to take into account additional load cases, which include evaluating the influence of unbalanced rotor aerodynamic loads caused by neighboring turbines' shade or wake effects on the global yawing moment.

Among the minimum required DLCs, DLC 1.6 and DLC 6.1 are deemed critical cases for analyzing mooring strength, drawing from the expertise of the oil and gas industry. DLC 1.6 encompasses the ultimate loading requirements resulting from normal turbulence model (NTM) and severe sea state (SSS) conditions, while DLC 6.1 incorporates the combination of extreme wind and wave conditions that combined recurrence period of 50 years. Since this thesis concentrates on examining the impact of clump weight on the entire system, DLC 6.1 is chosen as the focal DLC for this research.

The ABS guidelines recommend that DLC 6.1 ought to be simulated using either a three-hour simulation time with a fully coupled system in the time domain or frequency-domain analysis with dynamic effects. Additionally, it is advised to generate a minimum of six random seeds for a one-hour simulation time for each turbulent wind and sea state that is taken into account during the simulations.

doi:10.6342/NTU202303528

2.3 Design Basis

As the target location for this system is near Hsinchu offshore area, with an average water depth ranging from 60 m to 75 m, this study opts for a depth of 70 m since the mooring system is more crucial in shallower waters. In the case of FOWT, a dynamic cable is employed instead of static cable. Consequently, when designing the mooring systems, one must take into account the challenges associated with the curvature and compression issues of the dynamic cable. The displacement of the FOWT is constrained to ensure the practicality of the dynamic cable. In accordance with the manufacturer's guidelines [42], the maximum feasible diameter of the mooring chain to mass produce may be 178mm.

Design basis of the mooring system is shown:

- Water depth is assumed to be 70m
- The allowable platform offset is assumed to be 30% water depth in order to protect the dynamic cable.
- The mooring chain diameter should not be larger than 178mm (7 inches)

doi:10.6342/NTU202303528

2.4 Simulation Software

OrcaFlex, a commercial software package used for dynamic analysis of offshore systems, is mainly used in this thesis. OrcaFlex is a widely used software tool for simulating the dynamic behavior of floating structures, mooring systems, and other offshore systems under various environmental conditions.OrcaFlex uses a time-domain numerical simulation approach to model the dynamic behavior of offshore systems, taking into account the effects of waves, wind, currents, and other environmental loads on the system. It allows for the simulation of the dynamic response of FOWTs, including the motion, loads, and tensions in the mooring lines, as well as the structural behavior of the floating structure and other components of the wind turbine.

Besides OrcaFlex, OrcaWave is also used for the preliminary setup of the body type in OrcaFlex. OrcaWave is a diffraction analysis program that utilizes potential flow theory to compute the loading and response of submerged bodies caused by surface water waves.

doi:10.6342/NTU202303528

Chapter 3

Numerical Method

3.1 Diffraction Analysis

Full Quadratic Transfer Function (QTF) calculation is chosen in this study. Both potential formulation and source formulation is included. The Full QTF incorporates both the linear components and the quadratic components [43]. The fluid considered is assumed to be incompressible, inviscid and irrotational. The fluid velocity is expressed as

$$\bigtriangledown^2\Phi(X,t)=0 \tag{1}$$

where $\bigtriangledown\Phi$ is the gradient of the velocity potential , Φ is the velocity potential. Integrating the expression derived from substituting the fluid velocity into the Navier-Stokes equation results in the formulation of the Bernoulli equation, which relates the pressure distribution in the fluid.

$$p(X,t)=-\rho\left(\frac{\partial\Phi}{\partial t}+\frac{1}{2}(\bigtriangledown\Phi)^2+gZ\right) \tag{2}$$

Since wave steepness is typically small, perturbation expansion is employed.

$$\begin{aligned}\Phi(X,t)&=\Phi^{(1)}(X.t)+\Phi^{(2)}(X,t)+\ldots\\ p(X.t)&=p^{(0)}(X,t)+p^{(1)}(X,t)+p^{(2)}(X,t)+\ldots\end{aligned} \tag{3}$$

By solving the first-order problem $\Phi^{(1)}$, the response amplitude operators (RAOs), added mass, and damping could be determined. This provides insights into the behavior of the system under the influence of surface water waves. In full QTFs, the second order problem $\Phi^{(2)}$is also solved to determine wave drift load and sum frequency load.

doi:10.6342/NTU202303528

3.1.1 First Order Problem

Substituted $\Phi^{(1)}$ into the governing equations, only the first-order terms are retained, it leads to a linear boundary value problem for the first-order complex potential $\phi^{(1)}$, while $\phi^{(1)}$could be express as

$$\phi^{(1)} = \phi_I^{(1)} + \phi_S^{(1)} + \phi_R^{(1)} \tag{4}$$

where $\phi_I^{(1)}$is the potential of the incident wave, $\phi_S^{(1)}$is the scattered potential, due to the presence of a fixed obstructing entity, $\phi_R^{(1)}$ is the radiation potential, caused by first-order motion of the body in the fluid.

For the boundary condition in Orcawave, the velocity potential satisfies

$$\frac{\partial \Phi}{\partial Z} = 0 \tag{5}$$

on the seabed or as $Z \to -\infty$ in infinite depth water. When the wet surface of a rigid body moving with velocity U and angular velocity Ω at its instantaneous position, fluid velocity could be state as

$$n \cdot \bigtriangledown \Phi = n \cdot (U + \Omega \times X) \tag{6}$$

where n is unit normal. Meanwhile, the standard kinematic boundary condition of fluid dynamics is manifested on the free surface satisfy

$$\frac{\partial^2 \Phi}{\partial t^2} + g\frac{\partial \Phi}{\partial Z} + 2 \bigtriangledown \Phi \cdot \bigtriangledown \frac{\partial \Phi}{\partial t} + \frac{1}{2} \bigtriangledown \Phi \cdot \bigtriangledown (\bigtriangledown \Phi)^2 = 0 \tag{7}$$

$$\eta(X, Y, t) = -\frac{1}{g}\left(\frac{\partial \Phi}{\partial t} + \frac{1}{2} \bigtriangledown \Phi^2\right)\Big|_{Z=\eta} \tag{8}$$

where the instantaneous free surface $Z = \eta(X, Y, t)$ is determined by the Bernoulli equation.

doi:10.6342/NTU202303528

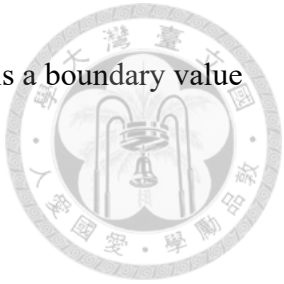

In first-order complex potential $\phi^{(1)}$, every component fulfills a boundary value problem by the following general formula

$$\begin{aligned} \nabla^2\phi &= 0 && X \in \nu \\ \frac{\partial\phi}{\partial n} &= q_B(X) && X \in S_B \\ g\frac{\partial\phi}{\partial Z} - \omega^2\phi &= q_F(X) && X \in S_F \\ \frac{\partial\phi}{\partial Z} &= 0 && Z \to -\infty (\text{or on seabed}) \end{aligned} \tag{9}$$

where the forcing functions q_B and q_F vary for each component in (4) and variable $\nu = \omega^2/g$ to simplify the subsequent equations. By (9), in finite water depth h, $\phi_I^{(1)}$ could be express as

$$\phi_I^{(1)}(X) = \frac{igA}{\omega} f(kZ) e^{-ik(X\cos\beta + Y\sin\beta)} \tag{10}$$

$$f(kZ) = \frac{\cosh\left(k(Z+h)\right)}{\cosh\left(kh\right)} \tag{11}$$

$$k\tanh kh = \nu \tag{12}$$

where A is height with dimensions of length, frequency ω, wavenumber k and wave heading β.

Boundary value problem in potential formulation is solved by the established boundary integral method with Green's theorem in global coordinate G_{XYZ}

$$2\pi\phi(X) + \int_{S_B} \phi(\xi)\frac{\partial G}{\partial n_\xi} dS_\xi = \int_{S_B} q_B(\xi) G dS_\xi + \int_{S_F} \frac{q_F(\xi)}{g} G dS_\xi \quad X \in S_B \tag{13}$$

where Green's theorem could express as

$$G(X,\xi) = \left[R^2 + (Z-\zeta)^2\right]^{-\frac{1}{2}} + \left[R^2 + (Z+\zeta+2h)^2\right]^{-\frac{1}{2}} + 2\int_0^\infty \frac{(k+\nu)\cosh k(z+h)\cosh k(\zeta+h)}{k\sinh kh + \nu\cosh kh} e^{-kh} J_0(kR)\, dk \tag{14}$$

$$R = \left[(X-\xi)^2 + (Y-\eta)^2\right]^{\frac{1}{2}}$$

doi:10.6342/NTU202303528

J_0 is the Bessel function of the first kind and the two vector arguments have coordinates $X = (\mathrm{X},\mathrm{Y},\mathrm{Z})$, $\xi = (\xi, \eta, \zeta)$, $\nu = \omega^2/g$, ω is the angular frequency of the wave and g is the acceleration due to gravity.

By making the assumption that $\phi^{(1)}$ remains constant within each mesh panel of S_B, (13) could be modified into a matrix equation that determines the potential value on each panel as

$$\begin{aligned}
\frac{1}{2}\phi_i^{(1)} + \sum_{P_j \in S_B} D_{ij}\phi_j^{(1)} &= \sum_{P_j \in S_B} S_{ij} q_{B,j} + \frac{1}{g}\sum_{P_j \in S_F} S_{ij} q_{F,j} \\
\phi_i^{(1)} &= \phi^{(1)}(C_i) \\
q_{B,i} &= q_{B,i}(C_i) \\
q_{F,i} &= q_{F,i}(C_i) \\
S_{ij} &= \frac{1}{4\pi}\int_{P_j} G(C_i, \xi) dS_\xi \\
D_{ij} &= \frac{1}{4\pi}\int_{P_j} \frac{\partial G}{\partial n_\xi}(C_i, \xi) dS_\xi
\end{aligned} \tag{15}$$

where P_i is the i^{th} panel, C_i is its centroid, S_{ij} and D_{ij} are influence matrices.

For source formulation, an indirect expression of the potentials $\phi_R^{(1)}$ and $\phi_S^{(1)}$ in terms of a source function $\sigma(X)$ is another consequence of Green's theorem.

$$2\pi\sigma(X) + \int_{S_B} \sigma(\xi)\frac{\partial G}{\partial n_x} dS_\xi = q_B(X) - \int_{S_F} \frac{q_F(\xi)}{4\pi g}\frac{\partial G}{\partial n_x} dS_\xi \qquad X \in S_\xi \tag{16}$$

A similar approach can be employed to discretize and numerically solve for σ in an analogous fashion to (12).

doi:10.6342/NTU202303528

3.1.2 Second Order Problem

Continue to second order, the forcing function now included nonlinear effects as

$$\Phi^{(2)}(X,t) = \sum_{ij} Re\Big\{ A_i A_j \phi_{ij}^{+}(X) e^{i(\omega_i+\omega_j)t} + A_i A_j^{*} \phi_{ij}^{-}(X) e^{i(\omega_i-\omega_j)t} \Big\} \tag{17}$$

when without loss of generality,

$$\begin{aligned} &\omega_i \geq \omega_j > 0 \\ &\phi_{ij}^{+}(X) = \phi_{ji}^{+}(X) \\ &\phi_{ij}^{-}(X) = \phi_{ji}^{-*}(X) \end{aligned} \tag{18}$$

where ω_i and ω_j are the frequencies of incident waves and $\omega_i \pm \omega_j$ are the frequencies at which second-order effects are excited. The linearity of the problem permits a breakdown of $\phi^{\pm}$ into distinct components as

$$\phi^{\pm} = \phi_I^{\pm} + \phi_R^{\pm} + \phi_S^{\pm} \tag{19}$$

Here, $\phi_I^{\pm}$ is the second-order potential in the absence of the body. $\phi_R^{\pm}$ is the potential due to the second-order body motion. $\phi_S^{\pm}$ is the remainder of $\phi^{\pm}$. The potentials $\phi_I^{\pm}$ and $\phi_S^{\pm}$ are required to evaluate the full QTFs on a body, but the second-order radiation potential $\phi_R^{\pm}$ is not required.

The incident and scattered potentials described in (19) both adhere (9). Thus, $\phi^{\pm}$ satisfy following equation,

$$\begin{aligned} \bigtriangledown^2 \phi^{\pm} &= 0 && X \in \nu \\ \frac{\partial \phi^{\pm}}{\partial n} &= q_B^{\pm}(X) && X \in S_B \\ g\frac{\partial \phi^{\pm}}{\partial Z} - (\omega_i+\omega_j)^2 \phi^{\pm} &= q_F^{\pm}(X) && X \in S_F \\ \frac{\partial \phi^{\pm}}{\partial Z} &= 0 && Z \to -\infty (\text{or on seabed}) \end{aligned} \tag{20}$$

doi:10.6342/NTU202303528

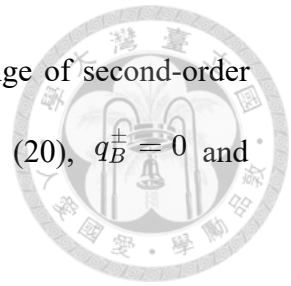

However, the forcing functions $q_B^{\pm}$ and $q_F^{\pm}$ now encompass a range of second-order effects. The incident wave potential, $\phi_I^{\pm}$, represents the solution (20), $q_B^{\pm} = 0$ and surface forcing is present. Thus,

$$
\begin{aligned}
q_F^{+}(X) = {} & \frac{\mathrm{i}}{4g}\omega_i\phi_i\left(-\omega_j^2\frac{\partial\phi_j}{\partial Z} + g\frac{\partial^2\phi_j}{\partial Z^2}\right) + \frac{\mathrm{i}}{4g}\omega_j\phi_j\left(-\omega_i^2\frac{\partial\phi i_j}{\partial Z} + g\frac{\partial^2\phi_i}{\partial Z^2}\right) \\
& - \frac{\mathrm{i}}{2}(\omega_i + \omega_j) \bigtriangledown \phi_i \cdot \bigtriangledown\phi_j^* \\
q_F^{+}(X) = {} & \frac{\mathrm{i}}{4g}\omega_i\phi_i\left(-\omega_j^2\frac{\partial\phi_j^*}{\partial Z} + g\frac{\partial^2\phi_j^*}{\partial Z^2}\right) + \frac{\mathrm{i}}{4g}\omega_j\phi_j^*\left(-\omega_i^2\frac{\partial\phi i_j}{\partial Z} + g\frac{\partial^2\phi_i}{\partial Z^2}\right) \\
& - \frac{\mathrm{i}}{2}(\omega_i - \omega_j) \bigtriangledown \phi_i \cdot \bigtriangledown\phi_j
\end{aligned}
\tag{21}
$$

where ϕ_i and ϕ_i represent the incident wave potentials of first-order at frequencies ωi and ωj respectively, the right-hand sides of equation (21) are computed at Z = 0.

On the other hand, the scattered potential, $\phi_S^{\pm}$, corresponds to the solution of (20) with the inclusion of body forcing as defined could be express as

$$
\begin{aligned}
q_B^{+} = {} & -\frac{\partial\phi_I^{+}}{\partial n} + \frac{1}{2}(\omega_i + \omega_j)n \cdot H^{+}x \\
& + \frac{1}{4}\{(\alpha_i \times n)\cdot(\mathrm{i}\omega_j d_j - \bigtriangledown\phi_j) + (\alpha_j \times n)\cdot(\mathrm{i}\omega_i d_i - \bigtriangledown\phi_i)\} \\
& - \frac{1}{4}n \cdot \left\{d_i \cdot \bigtriangledown \bigtriangledown \phi_j^* + d_j \cdot \bigtriangledown \bigtriangledown \phi_i\right\} \\
q_B^{-} = {} & -\frac{\partial\phi_I^{-}}{\partial n} + \frac{1}{2}(\omega_i - \omega_j)n \cdot H^{-}x \\
& + \frac{1}{4}\left\{(\alpha_i \times n)\cdot\left(-\mathrm{i}\omega_j d_j^* - \bigtriangledown\phi_j^*\right) + \left(\alpha_j^* \times n\right)\cdot(\mathrm{i}\omega_i d_i - \bigtriangledown\phi_i)\right\} \\
& - \frac{1}{4}n \cdot \left\{d_i \cdot \bigtriangledown \bigtriangledown \phi_j^* + d_j^* \cdot \bigtriangledown \bigtriangledown \phi_i\right\}
\end{aligned}
\tag{22}
$$

doi:10.6342/NTU202303528

where

$$
\begin{aligned}
H^{+} &= \mathcal{H}(\alpha_i, \alpha_j) \\
H^{-} &= \mathcal{H}\left(\alpha_i, \alpha_j^{*}\right) \\
\mathcal{H}(\alpha_i, \alpha_j) &= \frac{1}{2}\begin{pmatrix} -\alpha_{2i}\alpha_{2j} - \alpha_{3i}\alpha_{3j} & 0 & 0 \\ \alpha_{1i}\alpha_{2j} + \alpha_{2i}\alpha_{1j} & -\alpha_{1i}\alpha_{1j} - \alpha_{3i}\alpha_{3j} & 0 \\ \alpha_{1i}\alpha_{3j} + \alpha_{3i}\alpha_{1j} & \alpha_{2i}\alpha_{3j} + \alpha_{3i}\alpha_{2j} & -\alpha_{1i}\alpha_{1j} - \alpha_{2i}\alpha_{2j} \end{pmatrix}
\end{aligned} \tag{23}
$$

; x represents the position in body coordinates $Bxyz$. ϕ_i and ϕ_j denote the combined first-order potentials at frequencies ω_i and ω_j, respectively. ξ_i and α_i represent the complex displacement RAOs for translation and rotation. The function d_i can be defined as $\xi_i + \alpha_i \times x$.

doi:10.6342/NTU202303528

3.2 Dynamic Analysis

3.2.1 General

Equation of motion [43] for time domain could be express as

$$\overbrace{M(p,a)}^{\text{system inertia load}} + \underbrace{C(p,v)}_{\text{system damping load}} + \overbrace{K(p)}^{\text{system stiffness load}} = \underbrace{F(p,v,t)}_{\text{external load}} \tag{24}$$

where p, v, a, t are position, velocity, acceleration, simulation time respectively. The system geometry is recalculated at each time step, ensuring that the simulation accurately considers all geometric nonlinearities. This includes accounting for the spatial variation of both wave loads and contact loads.

In this study, explicit schemes, a semi-implicit Euler method with a fixed time step, is chosen. This calculation included forces and moments such as weight, buoyancy, hydrodynamic and aerodynamic drag, hydrodynamic added mass effects, tension and shear, bending and torque, seabed reaction and friction, contact forces with other objects and forces applied by links and winches. Then the equation of motion, based on Newton's law, is derived separately for each free body and line node, represented as

$$M(p)a \;=\; F(p,v,t) - C(p,v) - K(p) \tag{25}$$

Hydrodynamic load is based on Morison equation [44]

$$f = \underbrace{C_m \triangle a_f}_{\text{inertia}} + \underbrace{\frac{1}{2}\rho C_d A |v_{\mathrm{f}}| v_{\mathrm{f}}}_{drag} \tag{26}$$

where f is the fluid force per unit length on the body, C_m is the inertia coefficient for the body, $\triangle$ is the mass of fluid displaced by the body, a_f is the fluid acceleration relative to earth, ρ is the density of fluid, C_d is the drag coefficient for the body, A is the drag area, v_f is the fluid velocity relative to earth. When the body is moving, the

doi:10.6342/NTU202303528

inertia term $C_a \triangle a_b$ and the drag term changes to body-relative velocity, leading to an expanded version of Morison's equation (27) that is used in Orcaflex..

$$f = (C_m \triangle a_f - C_a \triangle a_b) + \frac{1}{2}\rho C_d A |v_\mathrm{r}| v_\mathrm{r} \tag{27}$$

In addition, C_a is the added mass coefficient for the body, a_b is the body acceleration relative to earth, v_r is the fluid velocity relative to the body.

3.2.2 Line

OrcaFlex utilizes a finite element model for a line where the line is divided into segments represented by straight massless model segments with nodes at each end shown in Figure 6.

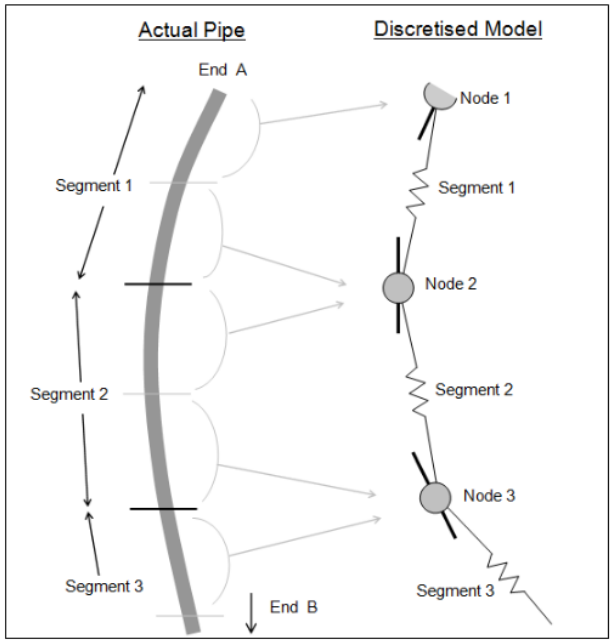

Figure 6. Finite element model of line in Orcaflex [44]

These segments focus on modeling the axial and torsional properties of the line, while other properties such as mass, weight, and buoyancy are lumped to the nodes. The nodes, sequentially numbered from end A to end B, effectively represent the two

doi:10.6342/NTU202303528

half-segments on either side, except for the end nodes which represent a single half-segment. The line model incorporates rotational spring-dampers for bending properties at each segment's ends, allowing for different bend stiffness values in orthogonal planes.

OrcaFlex calculates the tensions in segments by considering the distance and its rate of change between the nodes at the segment ends, as well as the axial direction represented by s_z. The tension in the axial spring-damper at the segment center is determined as a vector aligned with direction s_z, with its magnitude defined by the effective tension T_e while

$$T_e = T_w + (p_o a_o - p_i a_i) \tag{28}$$

where p_i, p_o represent internal and external pressure, a_i, a_o represent internal and external stress areas, T_w represent the wall tension. T_w in the context of linear axial stiffness consists of the following contributing factors

$$T_w = \overbrace{EA\epsilon}^{\text{axial stiffness}} - \underbrace{2\nu(p_o a_o - p_i a_i)}_{\text{pressure via the Poisson ratio effect}} + \overbrace{k_{tt}\frac{\tau}{l_0}}^{\text{torque coupling}} + \underbrace{EAc\frac{dl}{dt}\frac{1}{l_0}}_{\text{axial damping}} \tag{29}$$

Here, EA is axial stiffness, ϵ is total mean axial strain, l is instantaneous length of segment, l_0 is unstretched length of segment, ν is Poisson ratio, k_{tt} is tension/ torque coupling, τ is segment twist angle, c is damping coefficient in seconds, $\frac{dl}{dt}$ is the rate of increase of length.

Drag forces acting on a line are computed using the cross-flow principle, where the fluid velocity relative to the line v_r is split into its normal and parallel components v_n and v_z. As ρ be fluid density, p be proportion wet, $f_D = (f_{D_x}, f_{D_y}, f_{D_z})$ in local coordinates, drag force could be state as

doi:10.6342/NTU202303528

$$
\begin{aligned}
f_{D_x} &= \frac{1}{2} p \rho d_{\mathrm{n}} l C_{D_x} v_x |v_{\mathrm{n}}| \\
f_{D_y} &= \frac{1}{2} p \rho d_{\mathrm{n}} l C_{D_y} v_y |v_{\mathrm{n}}| \\
f_{D_z} &= \pm \frac{1}{2} p \rho \pi d_a l C_{D_z} |v|^2
\end{aligned} \tag{30}
$$

Meanwhile, the additional mass load on each line segment can be described using the inertia term of Morison's equation. Denoting the acceleration of the line segment relative to the earth, it can be express as

$$
f_A = C_m \triangle a_f - C_a \triangle a_{\mathrm{l}} \tag{31}
$$

where f_A is the added mass load on the line segment, $\triangle$ the mass of fluid displaced instantaneously by the segment, C_a is the *constant* added mass coefficient, $a_{\mathrm{f}}$is the fluid acceleration relative to earth, $a_{\mathrm{l}} = a_{\mathrm{f}} - a_{\mathrm{r}}$, a_{r} is the fluid acceleration relative to the line segment.

3.2.3 Clump Weights

A clump weight refers to a concentrated attachment that is connected to a specific node on a line, adding to its mass, buoyancy, and hydrodynamic force. It is heavy, constrained to move with the node and experiencing forces in a manner similar to a 3D buoy. Clump weights have only three translational degrees of freedom and their position is determined by the connecting node. They are assigned a height and offset, influencing their Z position for buoyancy and hydrodynamic force calculations. When the clump intersects the water surface, buoyancy and hydrodynamic forces are applied proportionally to the length of the clump submerged.

Drag forces of a clump weight are calculated as (32), while the calculation of the added mass contribution to clump inertia, AM, in each direction of the clump axis involves determining the value of (33).

doi:10.6342/NTU202303528

$$
\begin{aligned}
f_{D_x} &= -p_w \frac{1}{2} \rho C_{D_x} A_x v_x |v| \\
f_{D_y} &= -p_w \frac{1}{2} \rho C_{D_y} A_y v_y |v| \\
f_{D_z} &= -p_w \frac{1}{2} \rho C_{D_z} A_z v_z |v|
\end{aligned}
\tag{32}
$$

$$
\mathrm{AM} = p_{\mathrm{w}} \rho C_{\mathrm{a}} V \tag{33}
$$

3.2.4 Hydrodynamic Resistance

To model a more comprehensive and accurate assessment of the FOWT platform behavior, critical damping, yaw rate damping is considered additionally in this study.

3.2.4.1 Damping

Critical damping helps ensure the stability and response of the system by providing the necessary energy dissipation to prevent excessive oscillations. Critical damping in this study is calculated with a simplified equation

$$
\begin{aligned}
c_{\mathrm{c,heave}} &= 2 \times \sqrt{(m + m_{\mathrm{A,heave}}) k_{\mathrm{heave}}} \\
c_{\mathrm{c,roll}} &= 2 \times \sqrt{(m + m_{\mathrm{A,roll}}) k_{\mathrm{roll}}} \\
c_{\mathrm{c,pitch}} &= 2 \times \sqrt{(m + m_{\mathrm{A,pitch}}) k_{\mathrm{pitch}}}
\end{aligned}
\tag{34}
$$

where c_{c} is critical damping, $m$is system mass, $m_A$is added mass, k is stiffness.

3.2.4.2 Yaw Rate Drag

Yaw rate damping addresses the yaw motion of the floating offshore structure, helping to stabilize its orientation and minimize yaw-induced loads. Orcaflex employs formulas

doi:10.6342/NTU202303528

$$
\begin{aligned}
f_x &= \frac{1}{2}\rho|\omega|\omega K_{surge} \\
f_y &= \frac{1}{2}\rho|\omega|\omega K_{sway} \\
m_z &= \frac{1}{2}\rho|\omega|\omega K_{yaw}
\end{aligned} \tag{35}
$$

where ω is the yawing rate about the center, K_{surge}, K_{sway}, K_{yaw} is yaw drag factors, to model and simulate them Yaw rate drag in this study is based on an estimation method from [46].The sway drag load for each narrow vertical strip of the drag area is calculated in this approach by considering its area, the vessel's yaw rate, and an assumed drag coefficient. By integrating the contributions from all strips, the total sway force and yaw moment can be determined as

$$
m_z = \frac{1}{2}\rho\omega^2 C_D \frac{DL^4}{32} \tag{36}
$$

where D is draught, L is length between perpendiculars, C_D is the drag coefficient. Therefore, employing the strip theory concept for a slender ship with the hydrodynamic drag load originating at the center, allows us to make estimations of the drag factors for yaw rate by

$$
\begin{aligned}
K_{surge} &= 0 \\
K_{sway} &= 0 \\
K_{yaw} &= C_D \frac{DL^4}{32}
\end{aligned} \tag{37}
$$

doi:10.6342/NTU202303528

3.3 Environment

In this thesis, the research site chosen near the Hsinchu area relies on observation data obtained from the CWB Hsinchu Buoy. The Hsinchu Buoy is located approximately 3.5 km offshore from the Hsinchu Xiangshan Haishan Fishery Harbor, with a water depth of approximately 24.5 m [47]. The collected observation data includes various parameters such as wind speed, wave characteristics, currents, atmospheric pressure, sea temperature, and air temperature. These parameters are recorded at hourly intervals.

Specifically, wind speed data has been continuously recorded since April 1998, with measurements taken at two different heights: 2 m and 3 m. However, the majority of the data points are available at the 2 m height. Wave data has also been collected since 1998, but it was only starting from July 2001 that wave direction data became available.

3.3.1 Wind

The wind speed data used in the study is based on measurements at two different heights, 2 m and 3 m above sea surface, with preference given to the data measured at 2 m height. The wind speed data is then converted to hub height of a floating wind turbine (80 m) using the conversion formula recommended by IEC [41].

$$V(z) = V(z_r) \bullet \left(\frac{z}{z_r}\right)^{\alpha} \tag{28}$$

doi:10.6342/NTU202303528

which $V(z)$ is wind speed at elevation z, z_r is data height, 2 m in this case, α is wind shear coefficient referring to wind shear as suggested by IEC, 0.11 in this case.

Subsequently, a wind speed threshold of 35 m/s is selected [48], and wind speeds at the hub height that exceed this threshold are sorted in ascending order according to the recommendation by Gumbel.

$$F_j(x_j) = \frac{j}{n+1} \tag{29}$$

The cumulative probability F_j for each x_j is evaluated using the method suggested by Abild et al. [49] by sorting the data in ascending order, and then the Gumbel plot is used to display the return period of extreme wind speeds.

In order to make the simulation more realistic. Full field Wind allows for spatiotemporal variation of wind velocity, which could provide a realistic representation of the complex and dynamic behavior of wind in offshore environments. The IEC Kaimal model that was used in this study, as described in IEC 61400-1 [50], is based on the assumption of neutral atmospheric stability. It provides spectra for the three wind components, denoted as K (u, v, w) , and they are defined as follows:

$$S_K(f) = \frac{4\sigma_K^2 L_K/\overline{u}_{hub}}{(1+6fL_K/\overline{u}_{hub})^{5/3}} \tag{24}$$

where f is the cyclic frequency and L_K is an integral scale parameter,

$$L_K = \begin{cases} 8.1\Lambda_U, & K = u \\ 2.70\Lambda_U, & K = v \\ 0.66\Lambda_U, & K = w \end{cases} \tag{24}$$

turbulence scale, $\Lambda_U = 0.8 \cdot \min(60\text{m}, HubHt)$. The IEC Kaimal model assumes that the velocity spectra, along with their standard deviations, remain unchanged throughout the grid.

doi:10.6342/NTU202303528

3.3.2 Wave

Random waves, that may closely mimic natural phenomena that exhibit randomness, are considered in this study. Previous research [51] recommended using JONSWAP wave spectrum to modify Taiwan Strait's wave. The JONSWAP wave spectrum is a parametric model that defines the form of the wave spectrum curve. It is distinguished by a peak enhancement factor known as "γ," which signifies the amplification of wave energy within the peak frequency range. Spectrum for frequency $f \geq 0$ is given by the formula

$$S(f) = \frac{\alpha a_g^2}{16\pi^4} f^{-5} \exp\left[-\frac{5}{4}\left(\frac{f}{f_m}\right)^{-4}\right] \gamma^{\mathrm{b}} \tag{24}$$

where

$$\mathrm{b}=\exp\left[-\frac{1}{2\sigma^2}\left(\frac{f}{f_m}-1\right)^2\right] \tag{24}$$

$$\sigma\begin{cases}\sigma_1 & \text{for } f \leq f_{\mathrm{m}} \\ \sigma_2 & \text{for } f > f_{\mathrm{m}}\end{cases} \tag{24}$$

,f_m is peak frequency, a_g acceleration due to gravity γ, α, σ_1, σ_2 are data items.

3.3.3 Current

Power law method is used to simulate current profile. The current direction remains constant and does not change with depth. However, the current speed (S) varies with the position (X, Y, Z) according to the given formula

$$S = S_b + (S_{\mathrm{f}} - S_{\mathrm{b}})\left[\frac{Z - Z_b}{Z_{\mathrm{f}} - Z_b}\right]^{1/p} \tag{24}$$

doi:10.6342/NTU202303528

where S_{f} and S_{b} are the current speeds at the surface and seabed respectively, p is the power law exponent, Z_{f} is the Z coordinate of the still water level, Z_b is the Z coordinate of the seabed directly below (X,Y).

doi:10.6342/NTU202303528

Chapter 4

Model Setup

4.1 General Settings

In order to conduct a thorough examination of the entire FOWT system, time domain coupled simulation with a duration of 1 hour and a time step of 0.05 seconds is generated. Since the model exhibits symmetry on the x-z plane, environmental load directions ranging from 0° to 180° are considered, with intervals of 5°. The direction of wind, wave and current remain the same. Each model is simulated using 6 different initial conditions. Consequently, a total of 222 simulations are conducted for each case. All the results presented in this study represent the average values obtained from the 6 different seeds. Figure 7 shows the global coordinate and origin in the simulation with the origins located on the water plane of the platform.

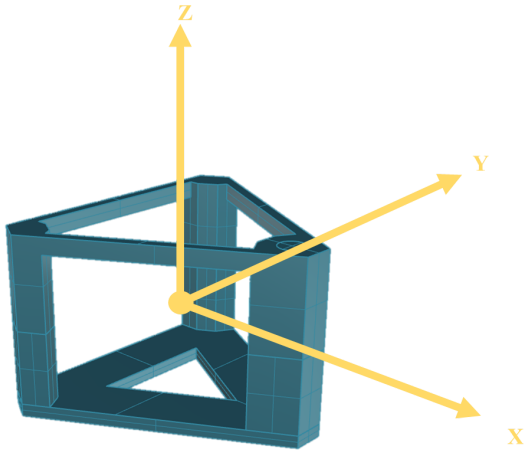

Figure 7. Global coordination and origin

doi:10.6342/NTU202303528

4.2 Wind Turbine

The wind turbine selected for this investigation is a scaled-down version of the NREL 5 MW Wind Turbine, based on the principles outlined of [52]. The specifications of the scaled down wind turbine are shown in Table 1. while the dimension is displayed in Figure 8. The aerodynamic properties of each blade of modeled wind turbine in this study is according to aerodynamic data provided NREL 5 MW [52]. The center of mass and principal inertia according to the setting of origin at the center of the circle of the tower base is given in Table 2.

Geometry profile data of modeled wind turbine blades is shown in Table 3. Eight distinct airfoil types had been integrated by research of NREL offshore 5-MW baseline wind turbines. The two innermost airfoil types correspond to cylinders without lift, having drag coefficients of 0.50 (Cylinder1) and 0.35 (Cylinder2). The corresponding airfoils aerodynamic data is shown in Figure 9.

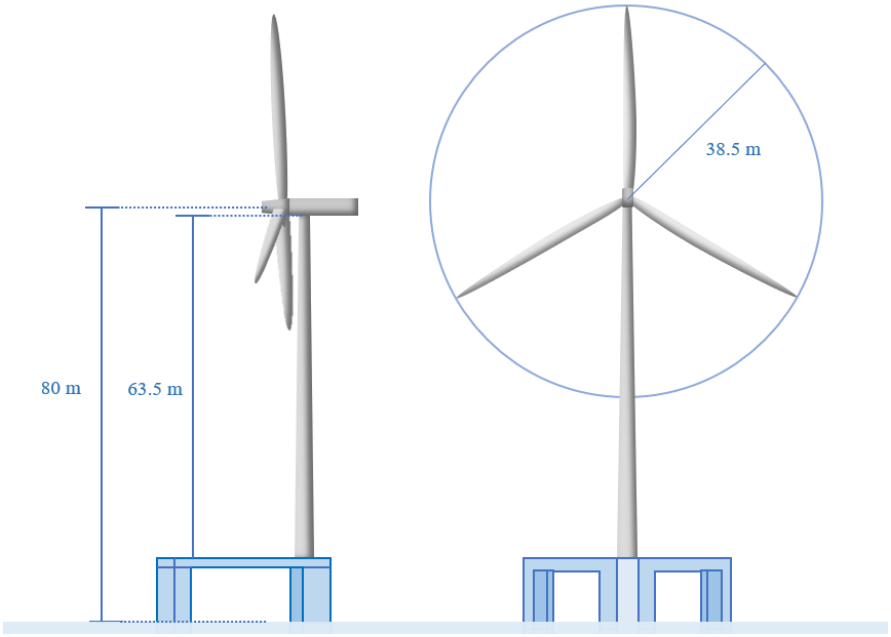

Figure 8. Dimension of modeled FOWT

doi:10.6342/NTU202303528

Table 1. Specification of modeled wind turbine

Rotor orientation, Configuration	Upwind, 3 Blades
Rotor Diameter	m
Hub height	80 m
Tower height	63.5 m
Tower Diameter (Top, Bottom)	2.5 m, 4.3 m
Tower Thickness (Top, Bottom)	18 mm, 32 mm
Blade mass	6.9 t
Tower mass	143.8 t
RNA mass	116.4 t
Pre-cone angle	2.5°

Table 2. Centre of mass and principal inertias of modeled 2 MW wind turbine

System		Turbine
Mass		298.7 t
Centre of mass (x, y, z) CM (m)		6.36E-03, 22E-09, 46.24
Principal inertia about centre of mass ($kg \bullet m^2$)	I_{xx}	1.67E+05
	I_{yy}	1.70E+05
	I_{zz}	7.61E+03
	I_{xy}	4.02E-01
	I_{yz}	-9.07E-02
	I_{zx}	-2.70E+01

doi:10.6342/NTU202303528

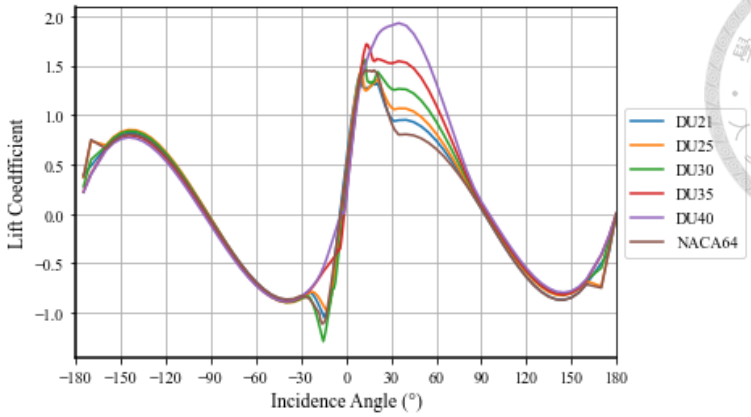

(a) Airfoil lift coefficient

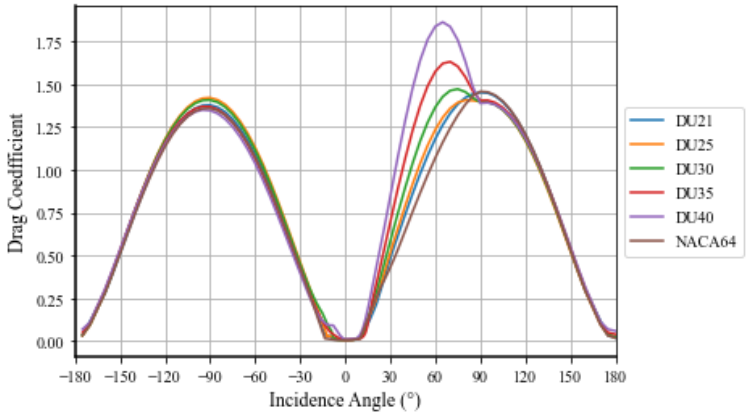

(b) Airfoil drag coefficient

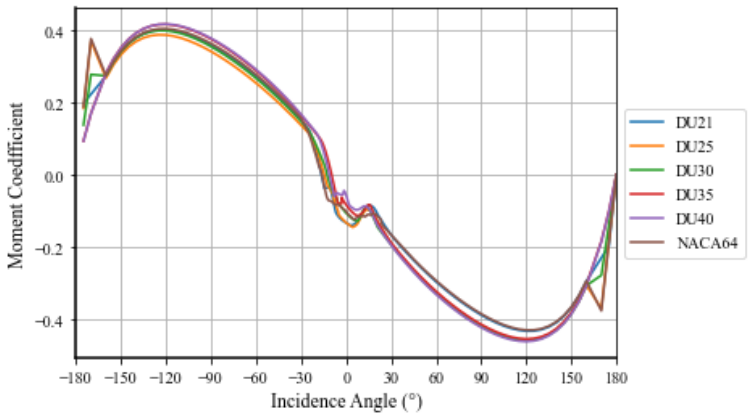

(c) Airfoil moment coefficient

Figure 9. Aerodynamic data

doi:10.6342/NTU202303528

Table 3. Blade geometry profile

Blade Fraction	Wing type	Chord (m)	Aerodynamic twist (deg)	Radius of gyration z (m)
0.044	Cylinder1	2.227	13.308	1.021
0.089	Cylinder1	2.412	13.308	0.983
0.133	Cylinder2	2.608	13.308	0.925
0.200	DU40	2.850	13.302	0.856
0.333	DU35	2.851	10.736	0.787
0.400	DU30	2.659	9.009	0.703
0.533	DU25	2.427	7.169	0.603
0.667	DU21	2.115	4.771	0.503
0.733	NACA64	1.884	3.144	0.483
0.800	NACA64	1.730	2.319	0.444
0.867	NACA64	1.576	1.526	0.407
0.911	NACA64	1.444	0.863	0.385
0.956	NACA64	1.294	0.370	0.328
1.000	NACA64	0.888	0.106	0.224

doi:10.6342/NTU202303528

4.3 Semi-submersible Platform

A 2 MW platform is used in this study. The platform consists of a ring pontoon that connects the columns and provides adjustable buoyancy. Three columns are placed on top of the ring pontoon to ensure stability, interconnected through bracing. The main column supports the wind turbine, while the side columns help maintain structural balance. All three columns are non-equilateral hexagonal.

The specifications of the 2 MW platform are detailed in Table 4, and the three view drawings are shown in Figure 10. Table 5 and Table 6 present the center of mass, principal inertias, and natural frequency of the 2 MW platform.

The local coordinate system of the platform is displayed in Figure 11, and the displacement response amplitude operator (RAO) of 6 degrees of freedom (6 DoF) after adding 3% critical damping in heave, roll, and pitch is shown in Figure 12. The inclusion of 3% critical damping is based on expert suggestions.

Table 7 and Table 8 provide the current load and wind load coefficients considered in this study. The current load and wind load coefficients are determined by calculating the platform's resistance due to current and wind from each direction, respectively. These resistances are implemented into the drag equation, following the description provided in the Orcaflex documentation, to obtain the corresponding coefficients.

doi:10.6342/NTU202303528

Table 4. Specification of modeled 2 MW platform

Length	40.8 m
Breath	47.1 m
Height	29.0 m
Draught	15.0 m
Pontoon width	9.0 m
Displacement	3895 t
Hull weight	±1000 t

Table 5. Centre of mass and principal inertias of 2 MW platform

System		Floater + Ballast + Turbine
Mass		3895 t
Centre of mass (x, y, z) CM (m)		2.33, 0, -3.26
Principal inertia about centre of mass $(kg \bullet m^2)$	I_{xx}	2.94E+06
	I_{yy}	3.11E+06
	I_{zz}	1.29E+06
	I_{xy}	-2.34E-08
	I_{yz}	-4.64E-07
	I_{zx}	-5.60E+05

doi:10.6342/NTU202303528

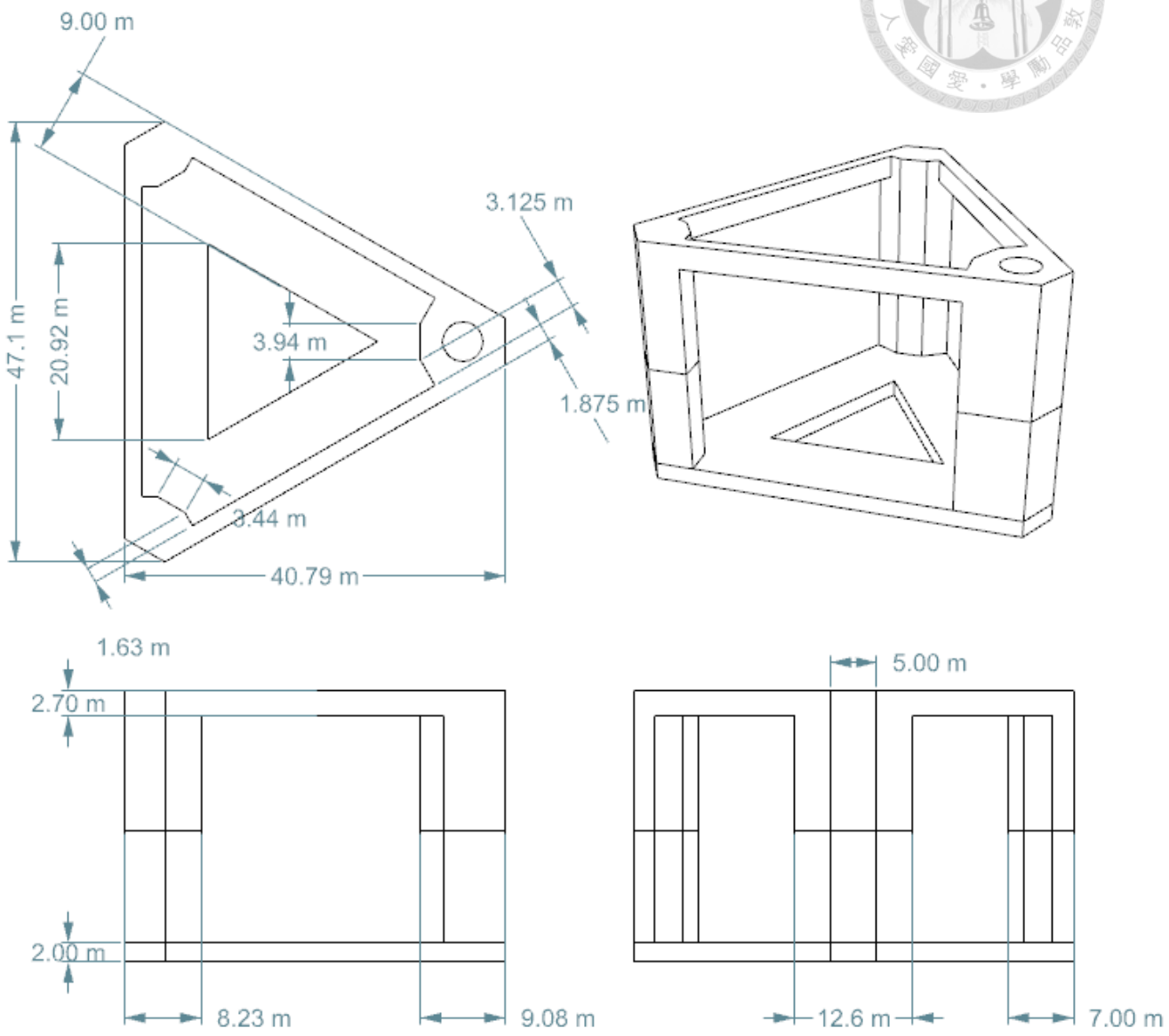

Figure 10. Three view drawing of 2 MW platform

doi:10.6342/NTU202303528

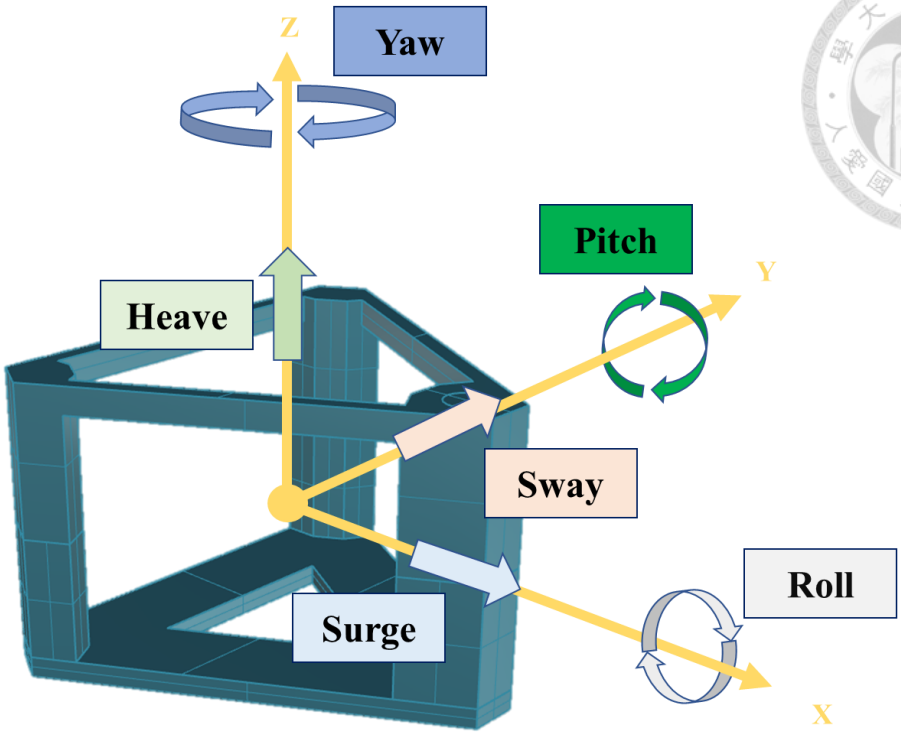

Figure 11. Local coordinate system of 2 MW platform

Table 6. Natural frequency of 2 MW platform

Degree of Freedom	Natural Frequncy (s)
Heave	17.8 / 30.5
Roll	42.5
Pitch	17.6 / 30.3

doi:10.6342/NTU202303528

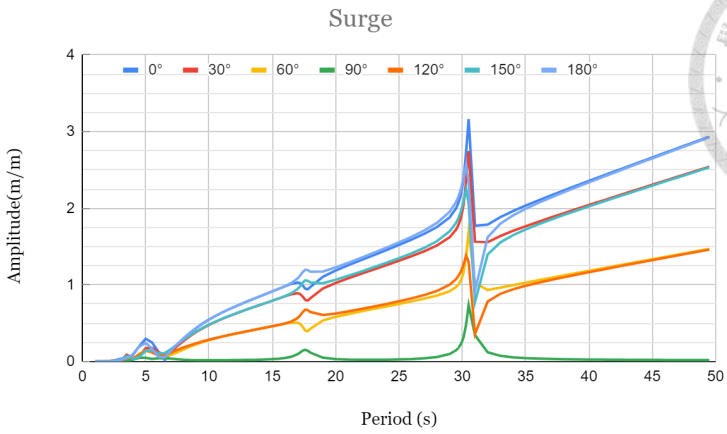

(a) Surge RAO of 2 MW platform

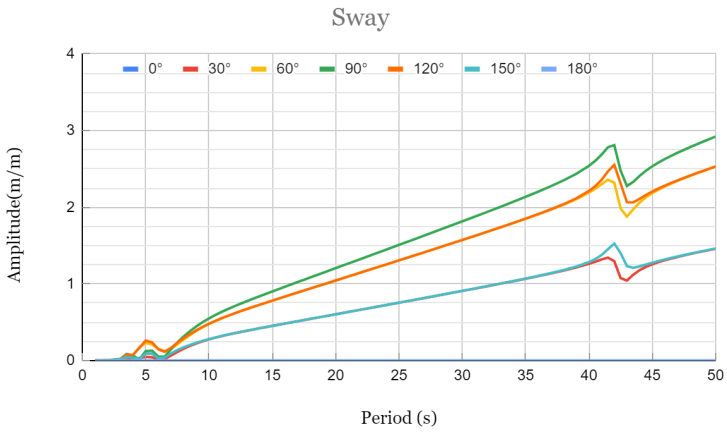

(b) Sway RAO of 2 MW platform

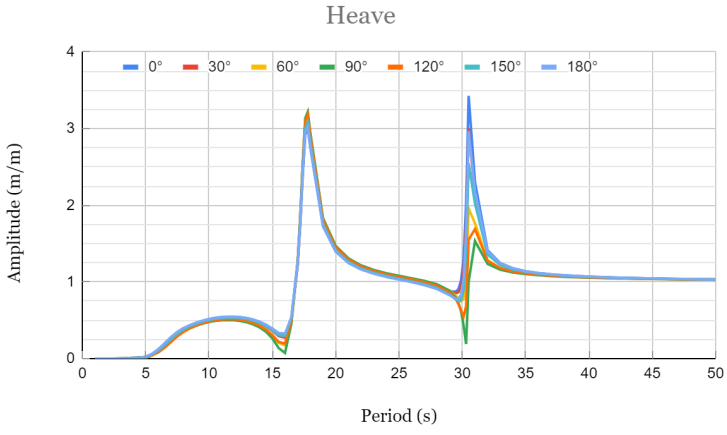

(c) Heave RAO of 2 MW platform

doi:10.6342/NTU202303528

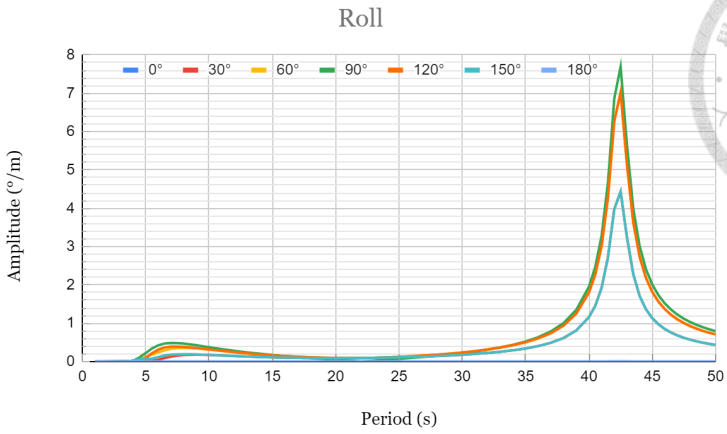

(d) Roll RAO of 2 MW platform

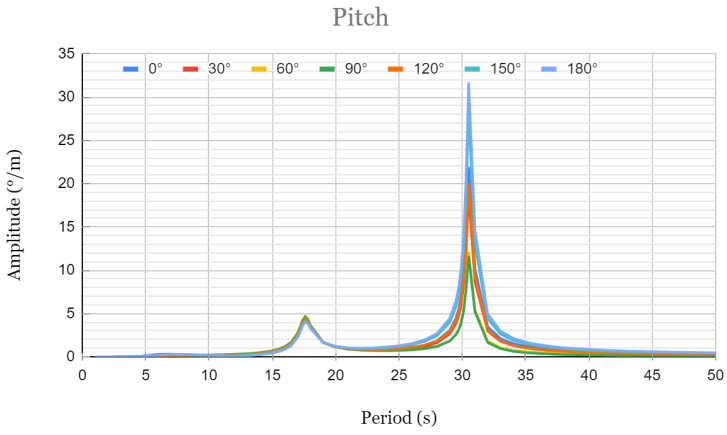

(e) Pitch RAO of 2 MW platform

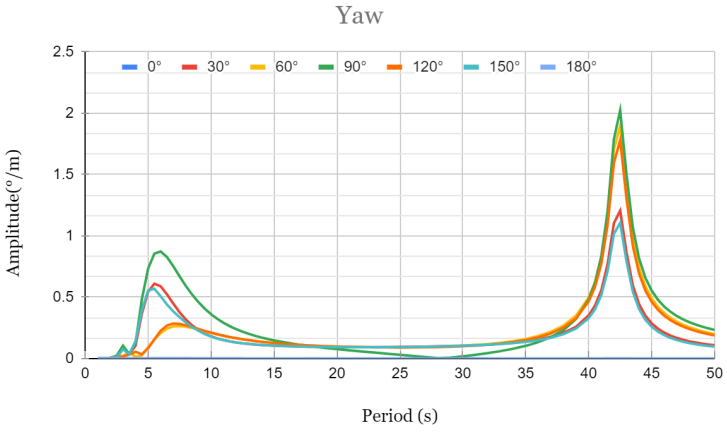

(f) Yaw RAO of 2 MW platform

Figure 12. Displacement RAO of 2 MW after adding 3% critical damping

doi:10.6342/NTU202303528

Table 7. Wind load coefficient

Direction	Surge	Sway	Heave	Roll	Pitch	Yaw
0°	1.477	-0.005	-0.001	0.001	0.014	0.002
30°	1.487	0.294	0.007	0.013	0.086	-0.010
60°	0.547	1.518	-0.002	0.008	-0.019	0.034
90°	-0.494	1.164	0.009	0.275	-0.019	0.009
120°	-0.720	1.838	0.005	0.008	0.005	0.038
150°	-1.166	0.799	0.012	0.145	0.070	0.052
180°	-1.153	-0.003	0.018	-0.001	-0.032	0.000

Table 8. Current load coefficient

Direction	Surge	Sway	Heave	Roll	Pitch	Yaw
0°	1.280	-0.002	-0.001	-0.001	-0.013	-0.003
30°	1.315	0.168	0.000	-0.008	0.127	-0.048
60°	0.362	1.235	0.000	0.008	0.032	0.163
90°	-0.573	1.001	0.008	0.028	0.039	0.158
120°	-0.608	1.649	0.001	0.019	-0.046	0.095
150°	-0.883	0.649	-0.001	0.015	0.071	0.158
180°	-0.896	-0.055	-0.006	-0.003	-0.175	0.011

doi:10.6342/NTU202303528

4.4 Mooring System

The primary focus of this study is to examine the impact of clump weight parameters on the entire mooring system of a 2 MW FOWT. Consequently, a relatively conservative mooring system is designed as the control case. The mooring system is designed with the design basis stated in Chapter 2. An all-chain catenary type 3x2 mooring arrangement is employed in this study. Geometry and properties of the modeling chain are shown in Figure 13 and Table 9, while the specification of the mooring system is shown in Table 10. Table 11. displays the coordinates of the fairlead and anchor locations. Additionally, Figure 15 provides a plan view of the mooring system, while the touchdown point is depicted in Figure 14.

The control case exhibits a maximum line tension of 14084 kN under extreme environmental load, with a safety factor of 1.71 in the intact condition which satisfies the industry guidelines [40]. The maximum offset of the control case is 13.94 m, which meets the requirement of 30% of the water depth which is 21 m. Figure 16 shows the restoring force of the mooring system of the control case mooring system.

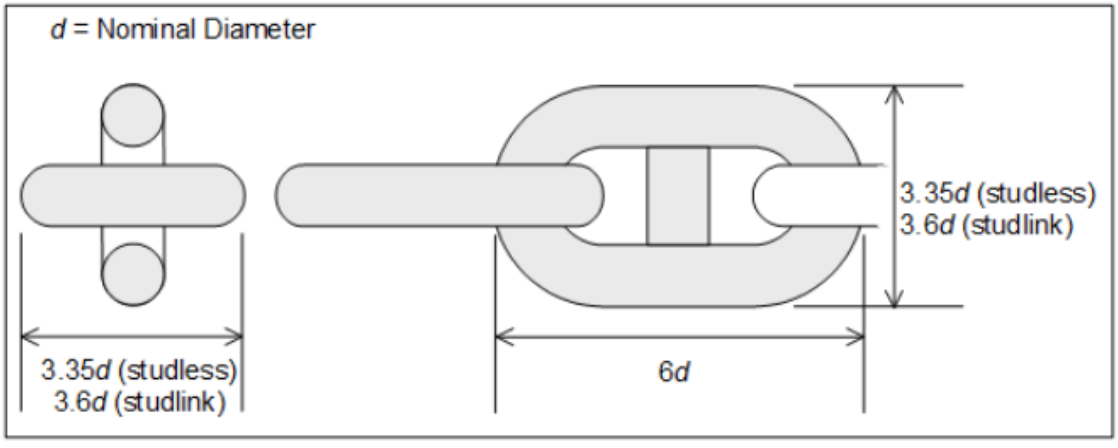

Figure 13. Geometry of modeling chain

doi:10.6342/NTU202303528

Table 9. Properties of modeling chain

Chain type	Studless Chain
Chain grade	R4S
Outer diameter	0.165 m
Mass/ length	0.545 t/m
Axial stiffness	2.325E+06 kN/m
Normal drag coefficient	2.4
Axial drag coefficient	1.15
Normal added mass coefficient	1.0
Axial added mass coefficient	0.5
Maximum breaking load	22976 kn

Table 10. Specification of designed mooring system

Mooring system type	All chain (studless)
Mooring pattern	Catenary
Anchor radius	900 m
Mooring line length	835.5 m
Pretension	1831 kN (7.97%)
Departure angle	30.9°

doi:10.6342/NTU202303528

Table 11. Coordinates of fairlead and anchor (in meter)

	Fairlead coordinate	Anchor coordinate
Line 1	(27.0, 1.5, -12.3)	(886.58, 78.44, -73.13)
Line 2	(27.0, -1.5, -12.3)	(886.58, -78.44, -73.13)
Line 3	(-12.51, -23.67, -12.3)	(-380.36, -815.68, -73.13)
Line 4	(-14.24, -22.67, -12.3)	(-516.22, -737.24, -73.13)
Line 5	(-14.24, 22.67, -12.3)	(-380.36, 815.68, -73.13)
Line 6	(-12.51, 23.67, -12.3)	(-516.22, 737.24, -73.13)

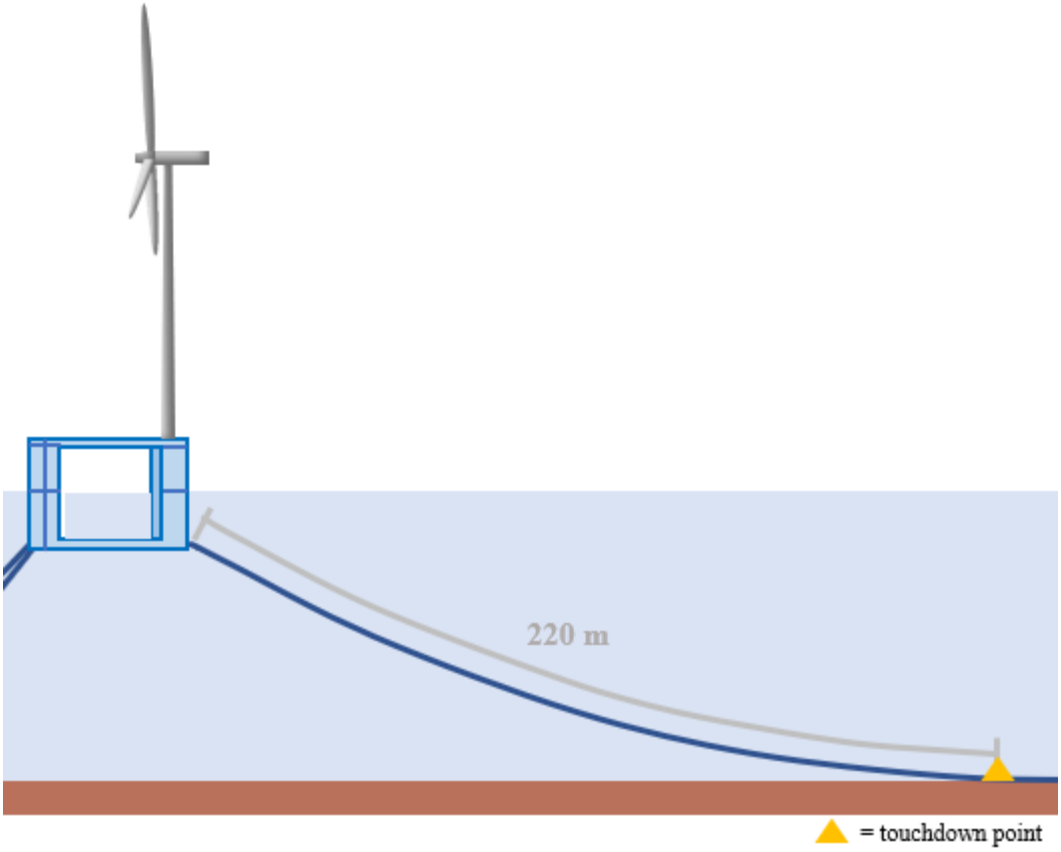

Figure 14. Touchdown point for designed mooring system

doi:10.6342/NTU202303528

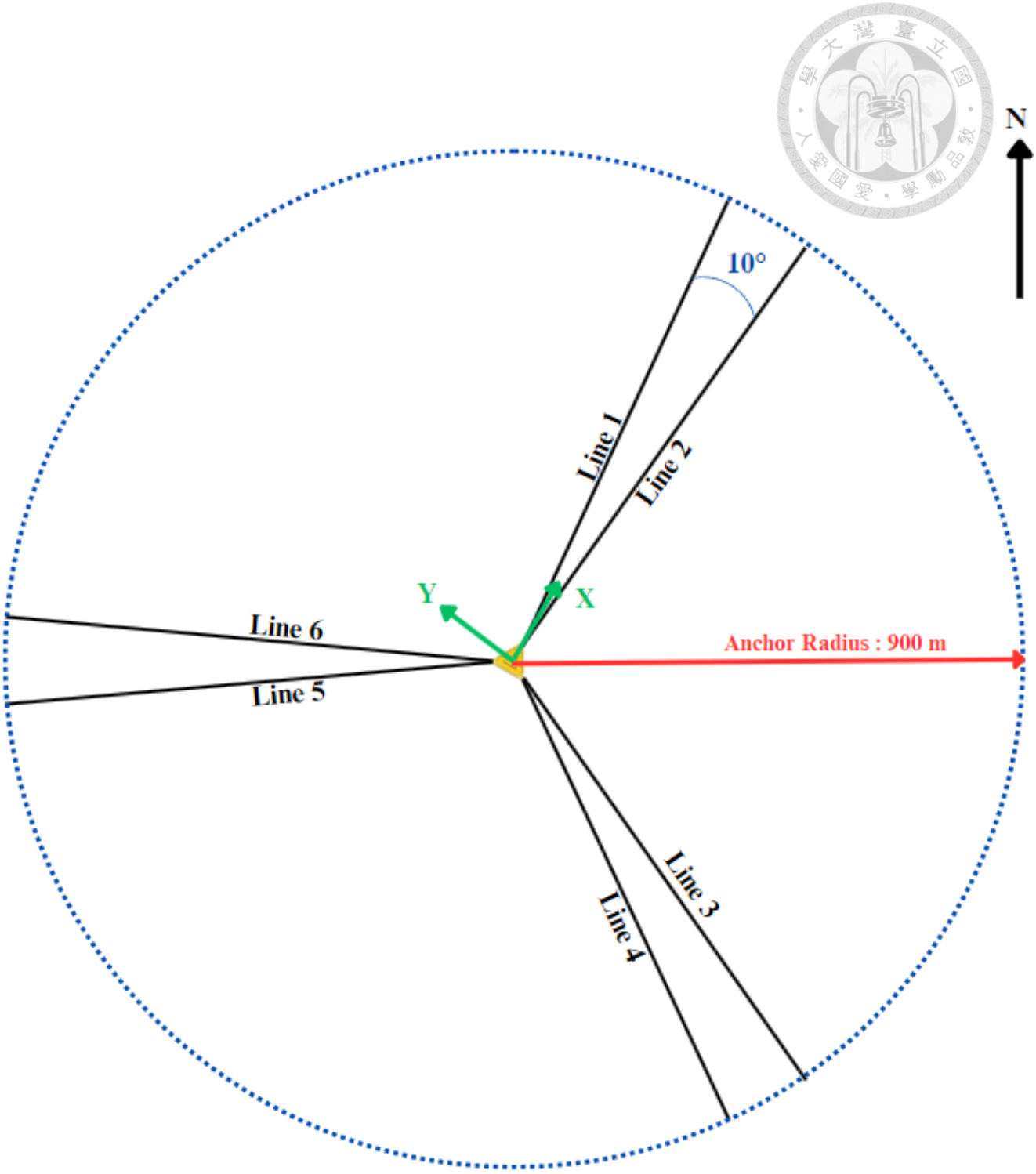

Figure 15. Plan view of model

doi:10.6342/NTU202303528

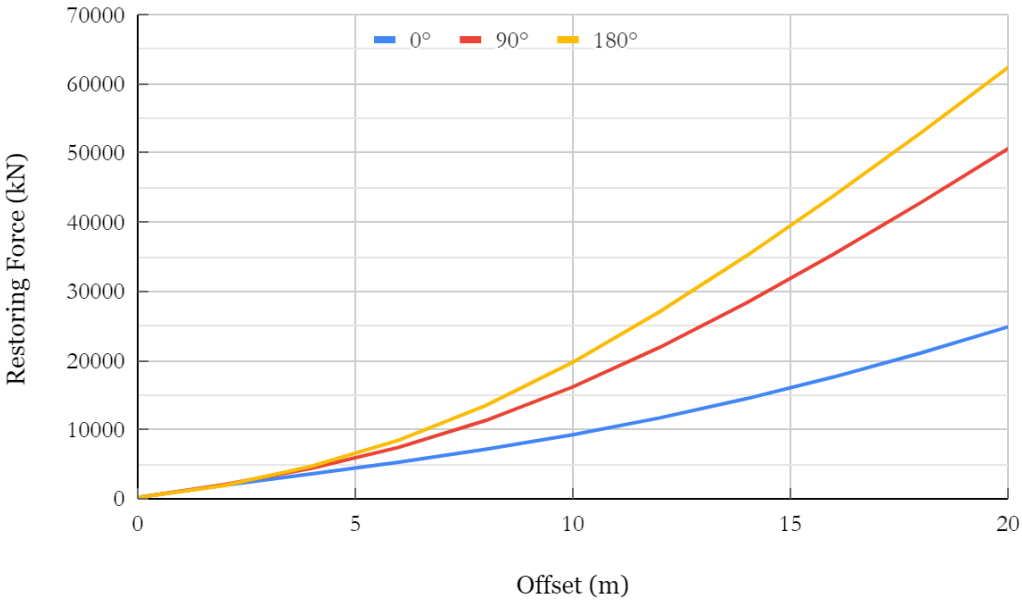

Figure 16. Restoring force for designed mooring system under control case

doi:10.6342/NTU202303528

4.5 Clump Weight

The clump weight utilized in this study is based on the reference [53] and depicted in Figure 17 with dimension state in Table 12. According to [34], the weight of the clump is not a crucial factor. By considering the feasibility of its installation, a clump weight of 3 tons with a height of 0.3 m has been selected. The properties of the modeled clump weight are presented in Table 13.

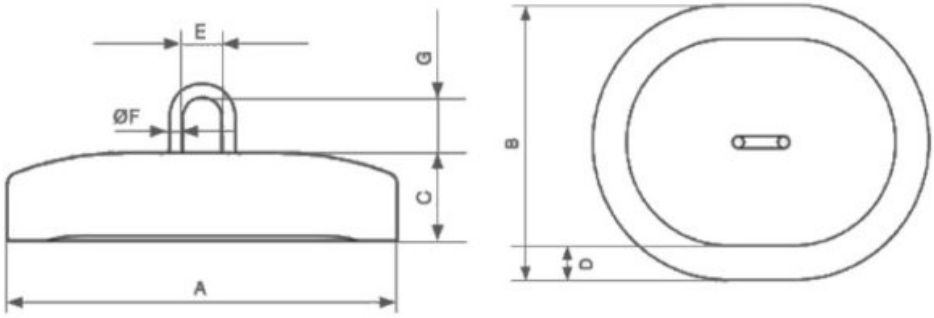

Figure 17. Dimension of reference clump weight

Table 12. Dimension of reference clump weight

	Dimension (m)
A	1.6
B	1.16
C	0.29
D	0.19
E	0.17
F	0.064
G	0.21

doi:10.6342/NTU202303528

Table 13. Properties of clump weight modeled

Mass	3 te
Volume	0.6 m
Height	0.3 m
Drag area	0.6 m^3
Drag coefficient	1.1
Added mass coefficient	1

doi:10.6342/NTU202303528

4.6 Environment

According to the design basis in Section 2.2, the environmental condition of regression 50 years is considered as the extreme sea state. The orientation of environmental loads is determined by the angle $\boldsymbol{\theta}$ in Figure 18, which measured counterclockwise from the positive x-axis. According to [51], JONSWAP wave spectrum with $\boldsymbol{\gamma}$ = 2.08 is appropriate to characterize waves in the Taiwan Strait which is shallow water. The Metocean conditions simulated in all instances within this thesis are outlined in Table 14. Figure 19 show the JONSWAP spectrum with $\boldsymbol{\gamma}$ = 2.08.

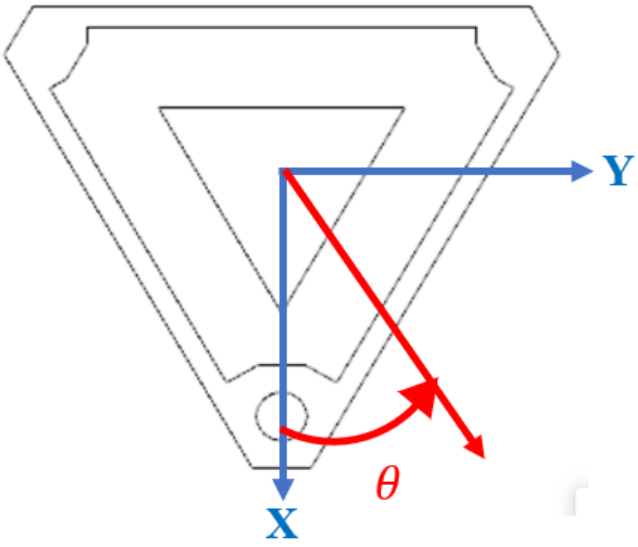

Figure 18. Environmental Load Direction

doi:10.6342/NTU202303528

Table 14. Metocean condition simulated

Wind	Wind spectrum	Full field wind
	Turbulence model	IEC-Kaimal
	Wind profile type	Power law
	Power law exponent	0.11
	Timestep	0.5 s
Wave	Wave spectrum	JONSWAP
	Peak enhancement factor, γ	2.08
	Significant wave height, H_s	12.72 m
	Wave period, T_p	11.8 s
Current	Current spectrum	Power law
	Current speed at seabed	0
	Current speed at water surface	1.59
	Power law exponent	7

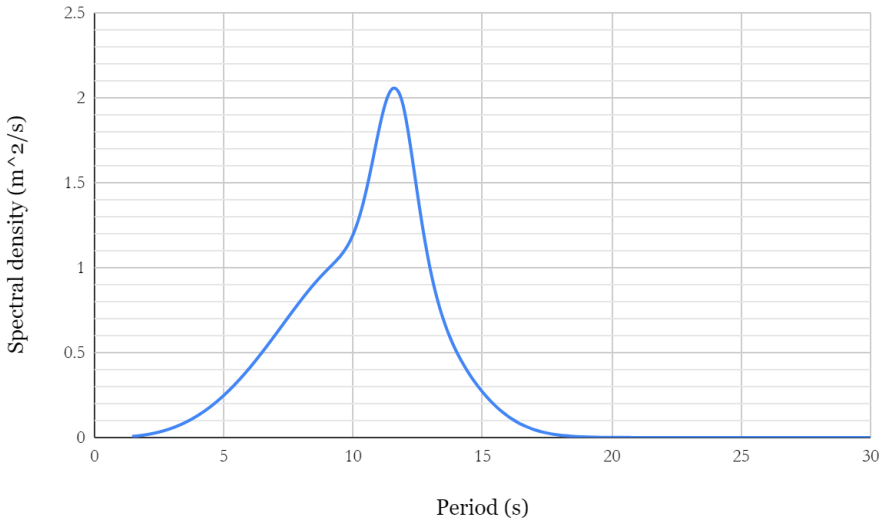

Figure 19. JONSWAP spectrum with γ = 2.08

doi:10.6342/NTU202303528

Chapter 5

Control case

5.1 Case Settings

The model test was conducted following the settings in Chapter 4, without considering clump weights. It involved a 2 MW platform and a wind turbine using a 3x2 all chain catenary mooring system. The environmental direction was simulated at angles ranging from 0° to 180°, with 6 simulations at each angle, increasing by 5° increments. The study's reported outcomes represent the average results obtained from the 6 simulations.

In DLC 6.1, the system encounters extreme sea state with a wind speed of 57 m/s at the hub height. Based on the wind turbine reference, the turbine is designed to be non-operational when the wind speed exceeds 25 m/s. As a result, the blades of the wind turbine in this study are fixed. Furthermore, in various simulations, the wind turbine blades are all pitched at a constant angle of 90°, and they consistently face the direction of environmental loads.

doi:10.6342/NTU202303528

5.2 6 Degree Motion (6 DoF)

Table 20. and Table 21. display the maximum and minimum values of surge, sway, and heave for each environmental load direction from 0° to 180°. It is evident that the highest maximum surge is observed at 0° and lowest at 90°, which align with the positive x-axis and are perpendicular to it, respectively. This observation is logical since 0° is along the positive x-axis and has bigger resistance.

Regarding sway, the maximum value occurs at 120°, which lies between two clusters of mooring lines. Conversely, the minimum value is recorded at 65°, corresponding to the alignment with Line 6. Meanwhile, the primary influence on heave motion is the weight of the suspended mooring lines that form catenary curves, resulting in minimal variations in the direction of environmental load carriage.

Table 22. to Table 23. show the maximum and minimum value of roll, pitch and yaw for each environmental load direction from 0° to 180°. The peak roll angle was observed at 120°, while the peak pitch angle occurred at 180°. This is due to the environmental load direction at 120°, where wind, waves, and current directly impact one of the side columns and the main column with the installed wind turbine, creating an imbalance along the x-axis and resulting in the highest roll angle. On the other hand, at 180°, the wave first hits the main column with the wind turbine and then the two side columns, leading to the highest pitch angle.

In terms of yaw movement, minimal yaw is observed at 0° and 180° due to the system's complete symmetry at the x-z plane in these orientations. Additionally, a local minimum in yaw motion is evident at 115°, potentially influenced by the relative equilibrium between the force exerted on the main column and the forces acting on the two side columns.

doi:10.6342/NTU202303528

5.3 Line Tension

Table 24. shows the maximum line tension along mooring lines from 0° to 180°. The data demonstrates that at 0° and 180°, Line 1 and Line 2, Line 3 and Line 6, and Line 4 and Line 5 exhibit almost the same maximum line tension, respectively. This symmetry arises from the system's alignment with the x-axis. Considering only the mooring system, a similar situation would be expected at 120° since it lies between two clusters of mooring lines. Nevertheless, the presence of the wind turbine installed on the main column disrupts the system's symmetry at 120°, resulting in distinct conditions in that particular region.

The findings indicate that when the wind, wave, and current directions align at the midpoint of the mooring lines within a cluster, the maximum line tension is relatively high. Specifically, this occurs at angles of 60° and 180°. However, due to the system's symmetry at 180°, the maximum line tension is slightly lower compared to the tension at 60°. Consequently, among all directions, the control case exhibits the highest maximum line tension at 60°.

doi:10.6342/NTU202303528

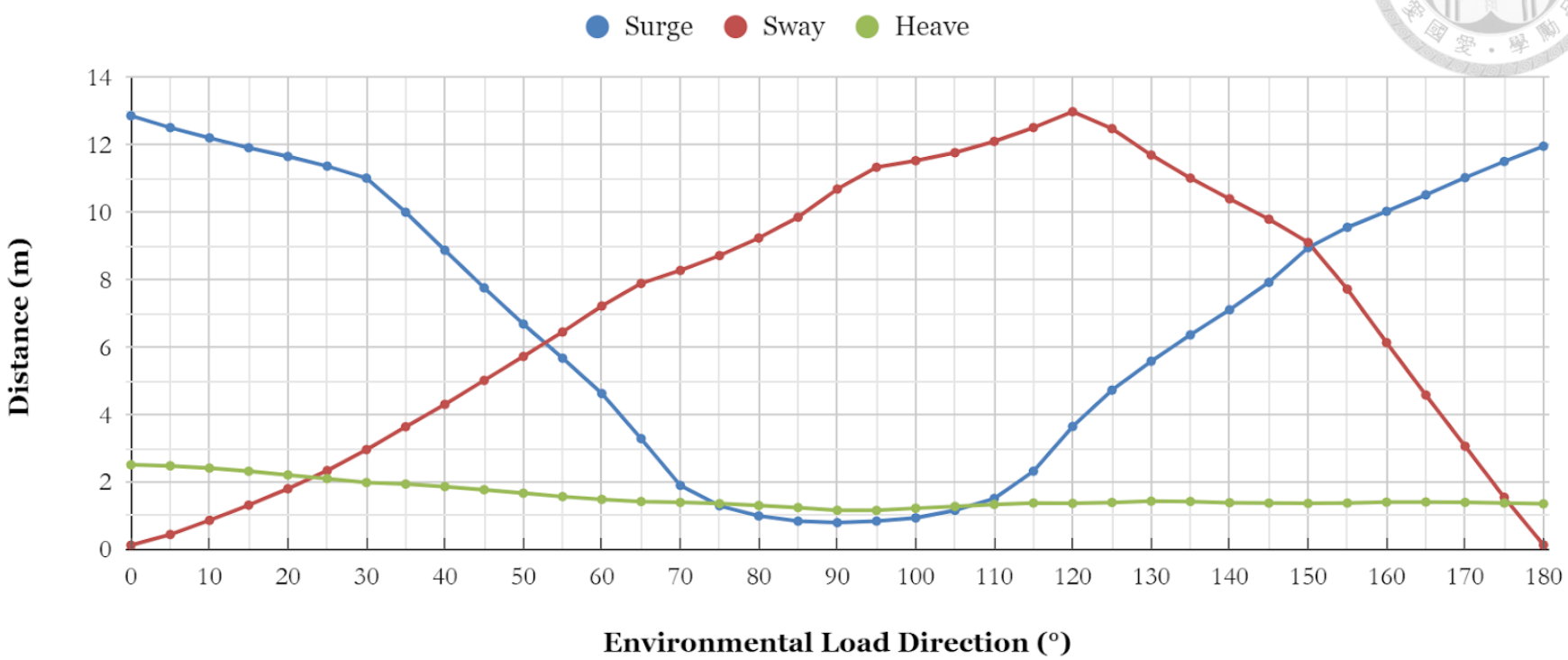

Figure 20. Maximum surge, sway, and heave motion of the control case in the direction from 0° to 180°

doi:10.6342/NTU202303528

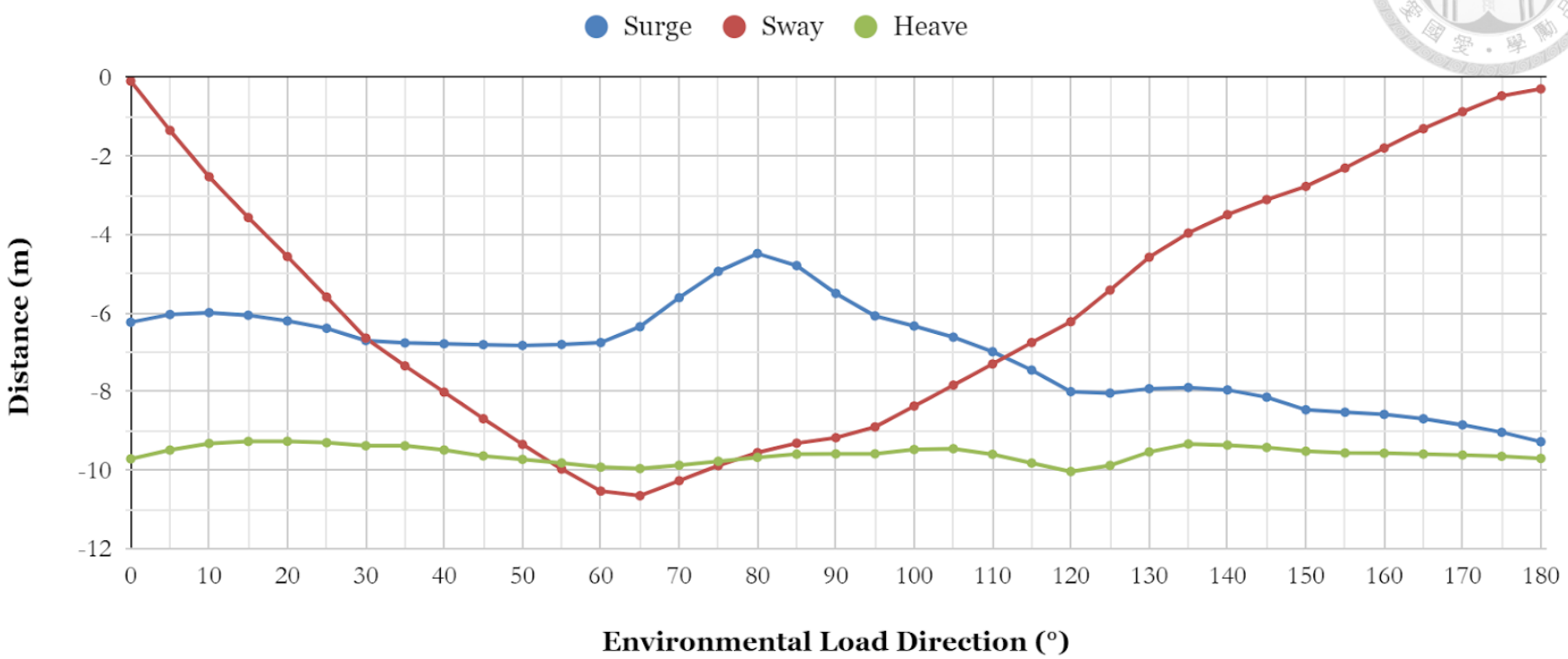

Figure 21. Minimum surge, sway, and heave motion of the control case in the direction from 0° to 180°

doi:10.6342/NTU202303528

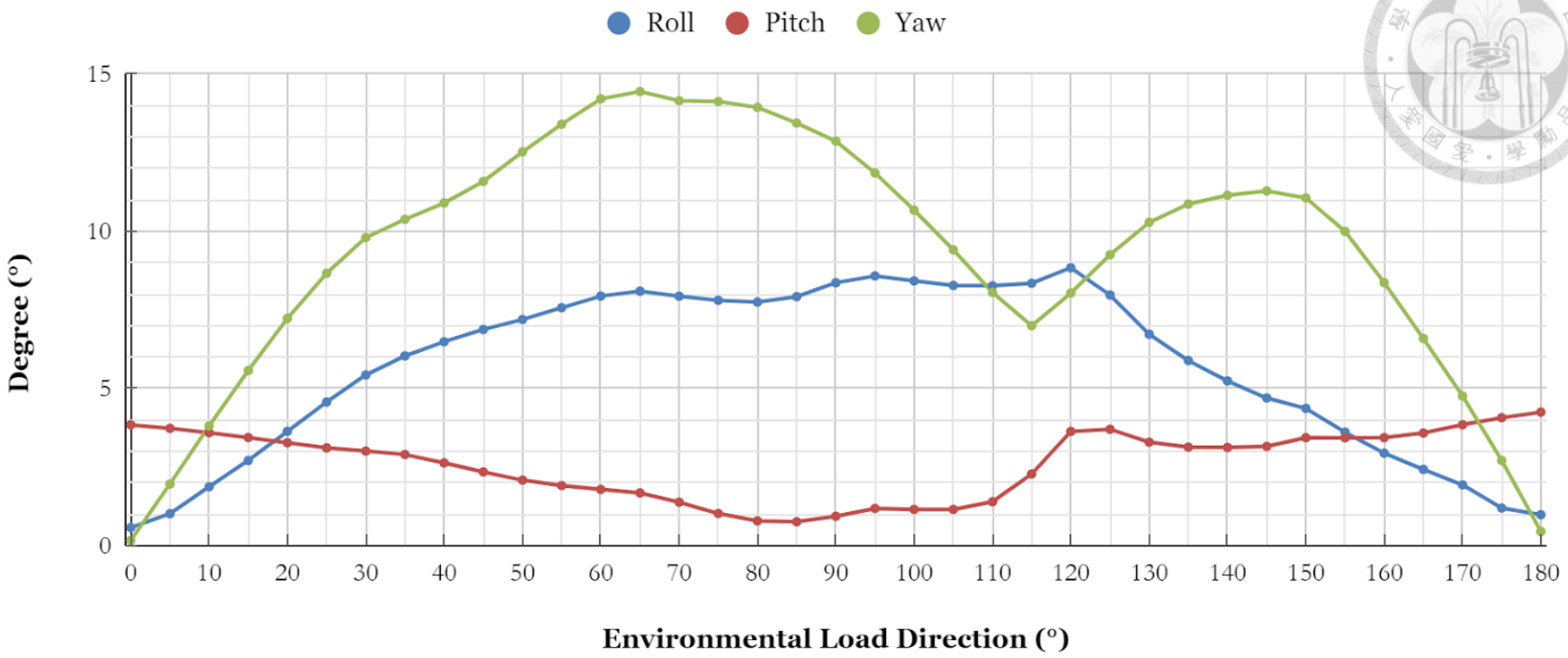

Figure 22. Maximum roll, pitch, and yaw motion of the control case in the direction from 0° to 180°

doi:10.6342/NTU202303528

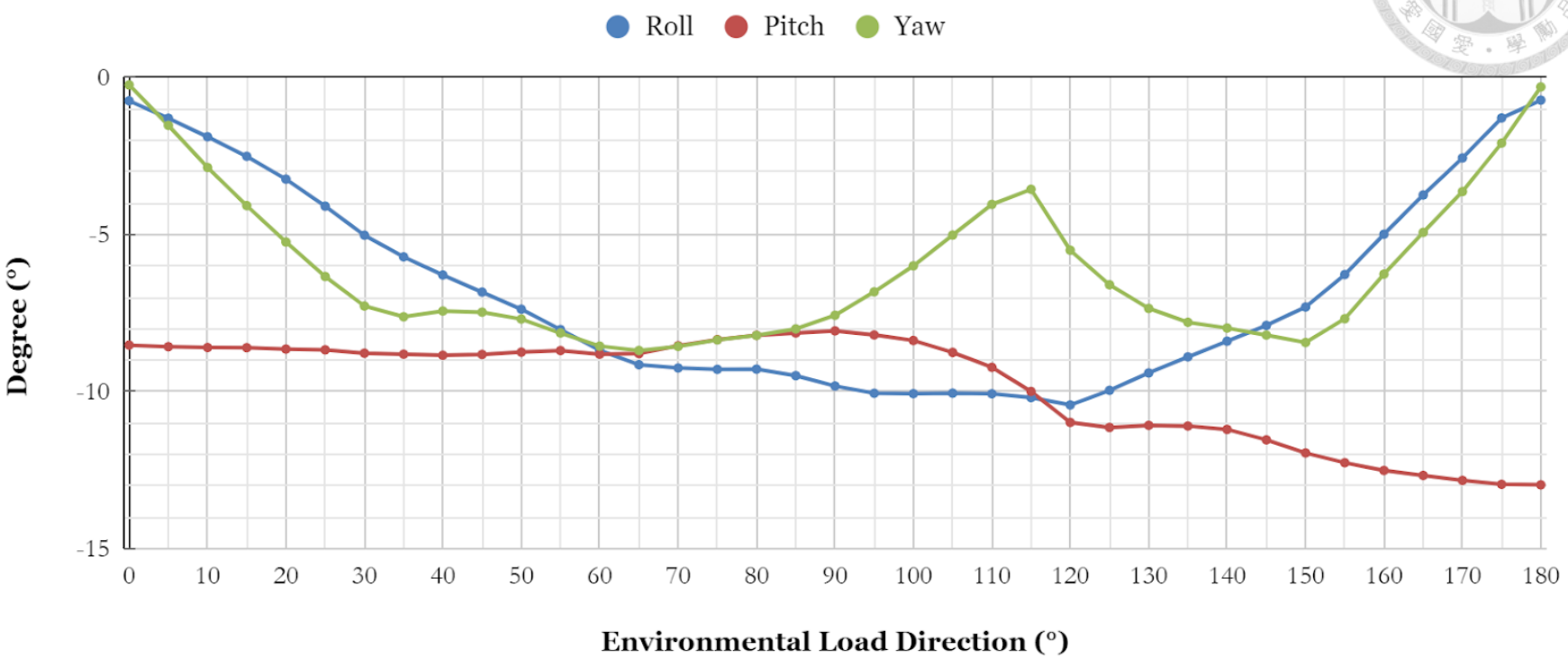

Figure 23. Minimum roll, pitch, and yaw motion of the control case in the direction from 0° to 180°

doi:10.6342/NTU202303528

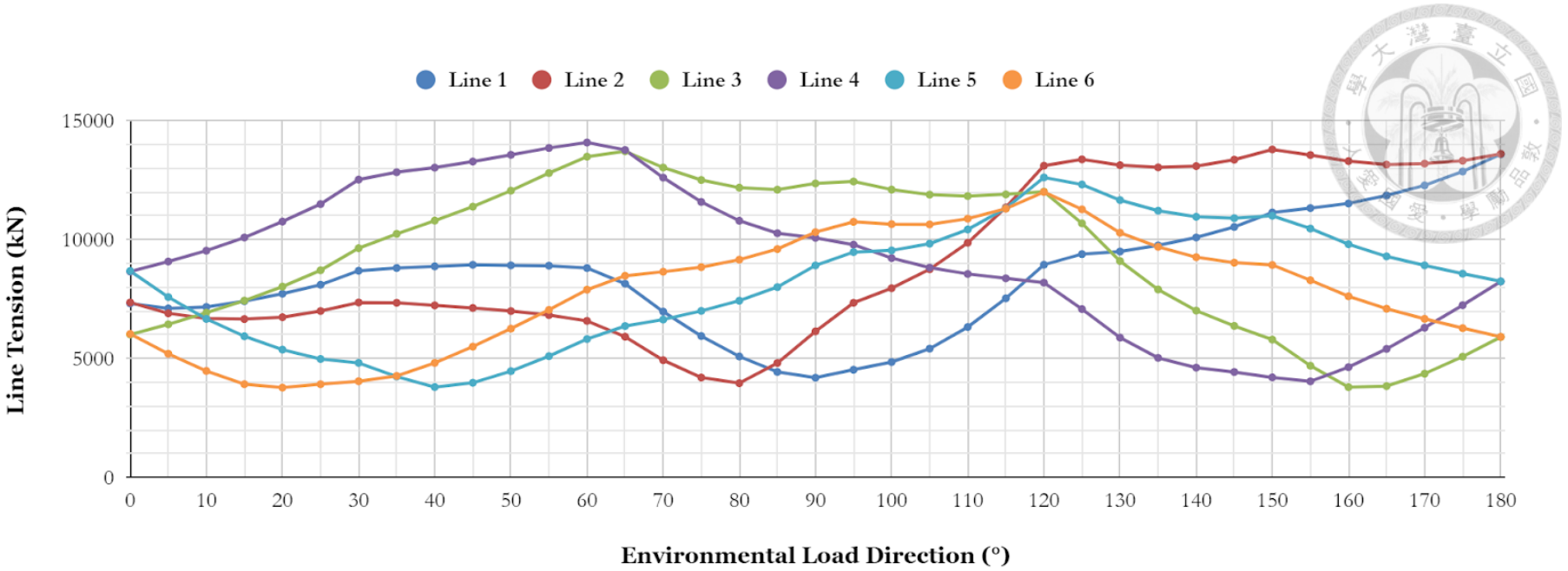

Figure 24. Maximum line tension along mooring lines of the control case in the direction from 0° to 180°

doi:10.6342/NTU202303528

5.4 Touchdown Point

Inspecting the touchdown point becomes essential in shallow water regions where the mooring lines may be unable to form the typical catenary profile or form a small angle between mooring line and sea surface due to restricted water depth. By verifying the touch down point, engineers can ensure proper anchoring and mitigate potential risks arising from the altered behavior of the mooring system in shallow water conditions.

The platform's maximum surge and sway do not exceed 14 m. Observations reveal that the platform moves along both the positive and negative x- and y-axes, with a range of 14 m from the origin. Inspection of the touchdown point for the mooring system during these movements is presented in Table 15. and Table 16..

The tables indicate significant variations in the touchdown point. Notably, Line 1 becomes most critical when the platform moves in the negative direction along the x-axis. When the platform moves 2 m in the negative x-axis direction, the touchdown point varies by 40.2 m along the arc length. This variation suggests that the mooring system's catenary shape is relatively oblique, resulting in a small angle between the mooring line and the sea surface. Although the mooring system theoretically provides a good restoring force, the mooring lines are susceptible to being pulled away from the seabed in this configuration.

doi:10.6342/NTU202303528

Table 15. Touchdown point of each line vary along x-directional offset

Offset (m)	Touchdown point (m)					
	Line 1	Line 2	Line 3	Line 4	Line 5	Line 6
-14	672.7	672.7	160.6	140.6	140.6	160.6
-12	602.4	602.4	160.6	150.6	150.6	160.6
-10	522.1	522.1	170.7	160.6	160.6	170.7
-8	441.8	441.8	180.8	170.7	170.7	180.8
-6	371.5	371.5	190.8	180.8	180.8	190.8
-4	311.2	311.2	200.8	190.8	190.8	200.8
-2	261.0	261.0	210.8	210.8	210.8	210.8
0	220.8	220.8	230.9	230.9	230.9	230.9
2	190.8	190.8	240.1	251.0	251.0	240.1
4	170.7	170.7	261.0	271.1	271.1	261.0
6	150.6	150.6	281.1	301.2	301.2	281.1
8	140.6	140.6	301.2	341.4	341.4	301.2
10	120.5	120.5	331.3	381.5	381.5	331.3
12	110.4	110.4	361.4	421.7	421.7	361.4
14	110.4	110.4	381.5	461.8	461.8	381.5

doi:10.6342/NTU202303528

Table 16. Touchdown point of each line vary along y-directional offset

Offset (m)	Touchdown point (m)					
	Line 1	Line 2	Line 3	Line 4	Line 5	Line 6
-14	250.0	210.8	110.4	120.5	592.3	642.5
-12	250.0	210.8	120.5	130.5	532.1	572.3
-10	241.0	210.8	130.5	140.6	461.8	502.0
-8	241.0	210.8	14.0.6	150.6	401.6	431.7
-6	230.9	210.8	160.6	160.6	351.4	361.4
-4	230.9	220.9	180.7	180.7	301.2	311.2
-2	230.9	220.9	200.8	200.8	261.0	261.0
0	220.8	220.8	230.9	230.9	230.9	230.9
2	220.9	230.9	261.0	261.0	200.8	200.8
4	200.9	231.0	311.2	301.2	180.7	180.7
6	210.8	230.9	361.4	351.4	160.6	160.6
8	210.8	241.0	431.7	401.6	150.6	140.6
10	210.8	241.0	502.0	461.8	140.6	130.5
12	210.8	241.0	572.3	532.1	130.5	120.5
14	210.8	241.0	642.5	592.0	120.4	110.4

doi:10.6342/NTU202303528

Chapter 6

Parametric Study

6.1 Clump Weight Starting Point

6.1.1 Case Settings

As the touchdown point for a no-clump FOWT system is around 220 m as shown in Figure 25., several cases before and after 220 m are investigated. Total 9 cases including a control case without any clump is stimulated. The cases S180, S190, S200, S210, S220, S230, S240, and S250 represent consecutive positions of the clump weight along the mooring line, starting from 180 meters and increasing by 10 meters in each subsequent case. Details of these cases are described in Table 17. where the side view of the starting points is shown in Figure 25. Average pretension of mooring lines in each case is shown in Table 18. It was observed that the variation in pretension could be attributed solely to the weight of the clump weights position before the touchdown point, thereby resulting in no substantial distinctions between the cases.

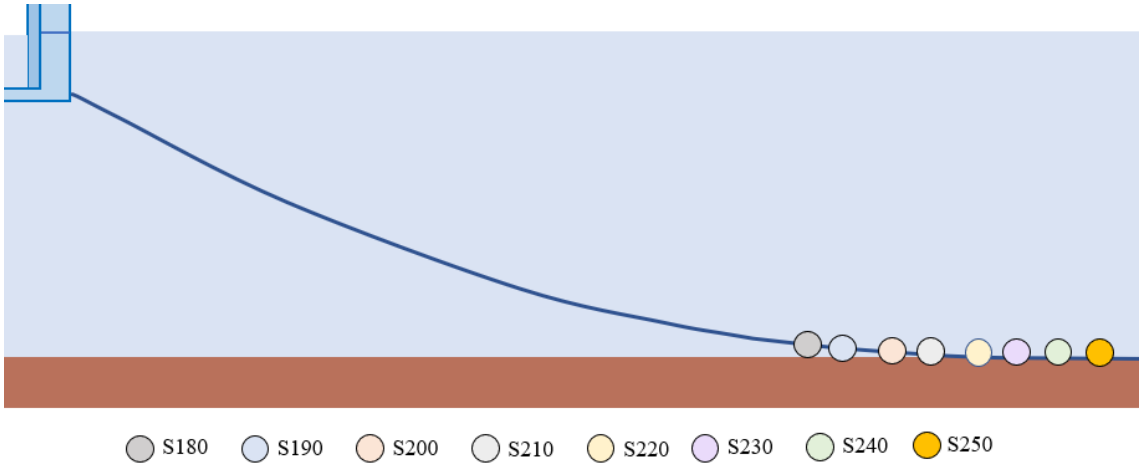

Figure 20. Side view of the starting point for S180, S190, S200, S210, S220, S230, S240 and S250 in Line 2

doi:10.6342/NTU202303528

Table 17. Cases for study clump weight starting position

Case		No Clump	S180	S190	S200	S210	S220	S230	S240	S250
Starting Point (m) (relative to End connect to platform's fairlead)			180 m	190 m	200 m	210 m	220m	230m	240m	250m
Clump Weight	Number	———	13							
	Weight		3 tons							
	Spacing		4 m							
	Volume		0.5 m^3							

Table 18. Average pretension of mooring lines in control case, S180, S190, S200, S210, S220, S230, S240, S250 and its difference with control case

Case	Pretension (kN)	Difference (%)
No clump	1831.77	0.00
S180	1896.29	3.52
S190	1864.28	1.77
S200	1848.25	0.90
S210	1843.07	0.62
S220	1841.87	0.55
S230	1841.30	0.52
S240	1841.05	0.51
S250	1840.87	0.50

doi:10.6342/NTU202303528

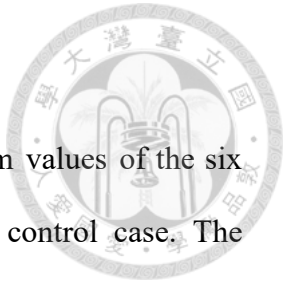

6.1.2 Result and Discussion

Table 19. and Table 27. display the minimum and maximum values of the six degrees of freedom (DoF) and their variances compared to the control case. The maximum surge value is 13.38 m, exhibiting a 3.94% increase, observed in case S180 at 0°. The highest sway value is 13.85 m, with a 6.51% difference, occurring in case S200 at 120°. The maximum roll value is 11.14°, demonstrating a 26.01% difference, observed in case S190 at 120°. The maximum pitch value is 5.61°, with a 32.05% difference, observed in case S190 at 120°. The maximum yaw value is 15.39°, indicating a 6.58% difference, observed in case S180 at 65°. The results indicate that after incorporating 13 clump weights, all six degrees of freedom experience an increase, particularly in roll and pitch.

Table 25 and Figure 26 provide information on the maximum tension experienced by the mooring lines in different scenarios. Upon adding the clump weight, Line 6 becomes the most tensioned line, exhibiting a 38.9% increase compared to the tension observed in the control case. Among the 9 cases, S190 represents the most challenging scenario, with Line 3, Line 4, Line 5 and Line 6 experiencing a rise of 20.1%, 22.3%, 26.2%, and 40.4% compared with line tension in the control case respectively. The reduction in the average difference of maximum line tension, compared to the control case, is observed as the starting position of the clump weight moves along the mooring line towards the anchor point.

Figure 23 shows the restoring force of direction 0°, 90° and 180° of cases. Compared to the restoring force of the control model, S180 and S250, restoring force would be slightly higher with the appearance of clump weights. Thus, the control case has the lowest restoring force while S180 has better restoring force when offset is lower and S250 has greater restoring force at bigger offset. A better restoring force in a

doi:10.6342/NTU202303528

mooring system typically results in lesser motion or reduced movement of the system but the result is exactly opposite thus the mooring system now may not be well designed. To investigate and understand this discrepancy, a parametric analysis is being conducted to identify the underlying factors causing the unexpected results.

Out of cases S180 to S250, S250 exhibits the most favorable scenario, but it is still inferior to the control case. Compared to cases where the starting positions are after the touchdown point, S180, S190, and S200 exhibit relatively poor performance. Therefore, in shallow water conditions with extreme sea states, it may be more advantageous to choose a starting position for the clump weight that is located after the touchdown point. Taking into account the motion and line tension of the FOWT system, S250 is selected for further investigation into the characteristics of the clump weight.

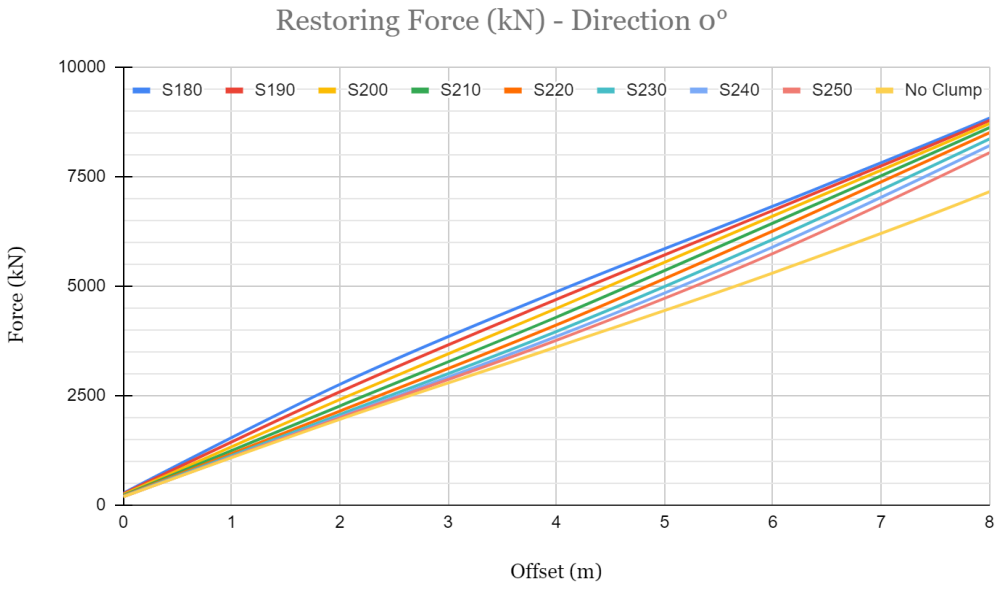

Figure 25. Restoring force of control case, S180, S190, S200, S210, S220, S230, S240 and S250.

doi:10.6342/NTU202303528

Table 19. Minimum and maximum value of surge for in control case, S180, S190, S200, S210, S220, S230, S240 and S250

	Min			Max		
	Direction (°)	Distance (m)	Difference (%)	Direction (°)	Distance (m)	Difference (%)
No Clump	180	-9.28	0.00	0	12.87	0.00
S180	180	-9.74	5.00	0	13.38	3.94
S190	180	-9.75	5.16	0	13.36	3.80
S200	180	-9.73	4.95	0	13.32	3.51
S210	180	-9.71	4.74	0	13.25	2.95
S220	180	-9.67	4.26	0	13.18	2.43
S230	180	-9.64	3.89	0	13.10	1.81
S240	180	-9.58	3.33	0	13.02	1.18
S250	180	-9.54	2.83	0	12.95	0.62

Table 20. Minimum and maximum value of sway in control case, S180, S190, S200, S210, S220, S230, S240 and S250

	Min			Max		
	Direction (°)	Distance (m)	Difference (%)	Direction (°)	Distance (m)	Difference (%)
No Clump	65	-10.65	0.00	120	12.99	0.00
S180	65	-11.06	3.86	120	13.80	6.22
S190	65	-11.08	4.04	120	13.83	6.51
S200	65	-11.10	4.20	120	13.85	6.60
S210	65	-11.11	4.24	120	13.81	6.35
S220	65	-11.09	4.05	120	13.76	5.96
S230	65	-11.07	3.91	120	13.68	5.32
S240	65	-11.03	3.57	120	13.58	4.53
S250	65	-11.02	3.43	120	13.49	3.85

doi:10.6342/NTU202303528

Table 21. Minimum and maximum value of heave in control case, S180, S190, S200, S210, S220, S230, S240 and S250

	Min			Max		
	Direction (°)	Distance (m)	Difference (%)	Direction (°)	Distance (m)	Difference (%)
No Clump	0	-9.96	0.00	0	2.51	0.00
S180	0	-10.66	7.03	0	2.23	-11.23
S190	0	-10.59	6.35	0	2.28	-9.30
S200	0	-10.51	5.53	0	2.32	-7.76
S210	0	-10.45	4.95	0	2.36	-6.20
S220	0	-10.37	4.18	0	2.39	-5.00
S230	0	-10.31	3.50	0	2.41	-4.06
S240	0	-10.25	2.88	0	2.44	-3.12
S250	0	-10.19	2.35	0	2.46	-2.36

Table 22. Minimum and maximum value of roll in control case, S180, S190, S200, S210, S220, S230, S240 and S250

	Min			Max		
	Direction (°)	Degree (°)	Difference (%)	Direction (°)	Degree (°)	Difference (%)
No Clump	120	-10.43	0	120	8.84	0.00
S180	120	-10.75	3.12	120	11.00	24.43
S190	120	-10.94	4.88	120	11.14	26.01
S200	120	-11.04	5.84	120	11.12	25.82
S210	120	-11.11	6.59	120	11.06	25.16
S220	120	-11.14	6.88	120	10.94	23.73
S230	120	-11.15	6.96	120	10.83	22.58
S240	120	-11.11	6.52	120	10.69	21.01
S250	120	-11.08	6.28	120	10.50	18.81

doi:10.6342/NTU202303528

Table 23. Minimum and maximum value of pitch in control case, S180, S190, S200, S210, S220, S230, S240 and S250

	Min			Max		
	Direction (°)	Degree (°)	Difference (%)	Direction (°)	Degree (°)	Difference (%)
No Clump	180	-12.97	0.00	180	4.25	0.00
S180	180	-12.98	0.09	120	5.61	32.12
S190	180	-12.97	0.05	120	5.61	32.05
S200	180	-12.96	-0.03	120	5.47	28.82
S210	180	-12.97	0.02	120	5.40	27.25
S220	180	-12.96	-0.04	120	5.27	24.09
S230	180	-12.98	0.07	120	5.14	20.93
S240	180	-12.98	0.14	125	5.02	18.13
S250	180	-12.99	0.15	125	4.87	14.64

Table 24. Minimum and maximum value of yaw in control case, S180, S190, S200, S210, S220, S230, S240 and S250

	Min			Max		
	Direction (°)	Degree (°)	Difference (%)	Direction (°)	Degree (°)	Difference (%)
No Clump	65	-8.68	0.00	65	14.44	0.00
S180	65	-9.24	6.40	65	15.39	6.58
S190	150	-9.17	5.51	65	15.27	5.74
S200	150	-9.17	5.54	65	15.09	4.49
S210	150	-9.20	5.99	65	14.91	3.21
S220	150	-9.18	5.67	65	14.74	2.08
S230	150	-9.16	5.51	65	14.64	1.34
S240	150	-9.07	4.45	65	14.53	0.57
S250	150	-8.99	3.54	65	14.44	-0.01

doi:10.6342/NTU202303528

Table 25. Maximum line tension along mooring lines in control case, S180, S190, S200, S210, S220, S230, S240 and S250

	Line 1		Line 2		Line 3		Line 4		Line 5		Line 6		Average Difference (%)
	Max Tension (kN)	Difference (%)	Max Tension (kN)	Difference (%)	Max Tension (kN)	Difference (%)	Max Tension (kN)	Difference (%)	Max Tension (kN)	Difference (%)	Max Tension (kN)	Difference (%)	
No Clump	13589	0.00	13794	0.0	13716	0.0	14084	0.0	12616	0.0	12004	0.0	0.0
S180	15448	13.68	15673	13.6	15551	13.4	16178	14.9	15767	25.0	16678	38.9	19.9
S190	15508	14.12	15806	14.6	16479	20.1	17228	22.3	15922	26.2	16854	40.4	23.0
S200	15305	12.63	15586	13.0	15577	13.6	16139	14.6	15435	22.3	14848	23.7	16.6
S210	15221	12.01	15520	12.5	15524	13.2	16080	14.2	15255	20.9	14632	21.9	15.8
S220	15109	11.19	15371	11.4	15447	12.6	16028	13.8	15041	19.2	14476	20.6	14.8
S230	14954	10.04	15263	10.6	15407	12.3	15897	12.9	14806	17.4	14228	18.5	13.6
S240	14829	9.13	15148	9.8	15216	10.9	15789	12.1	14662	16.2	14065	17.2	12.6
S250	14643	7.76	14901	8.0	15048	9.7	15738	11.7	14568	15.5	13831	15.2	11.3

doi:10.6342/NTU202303528

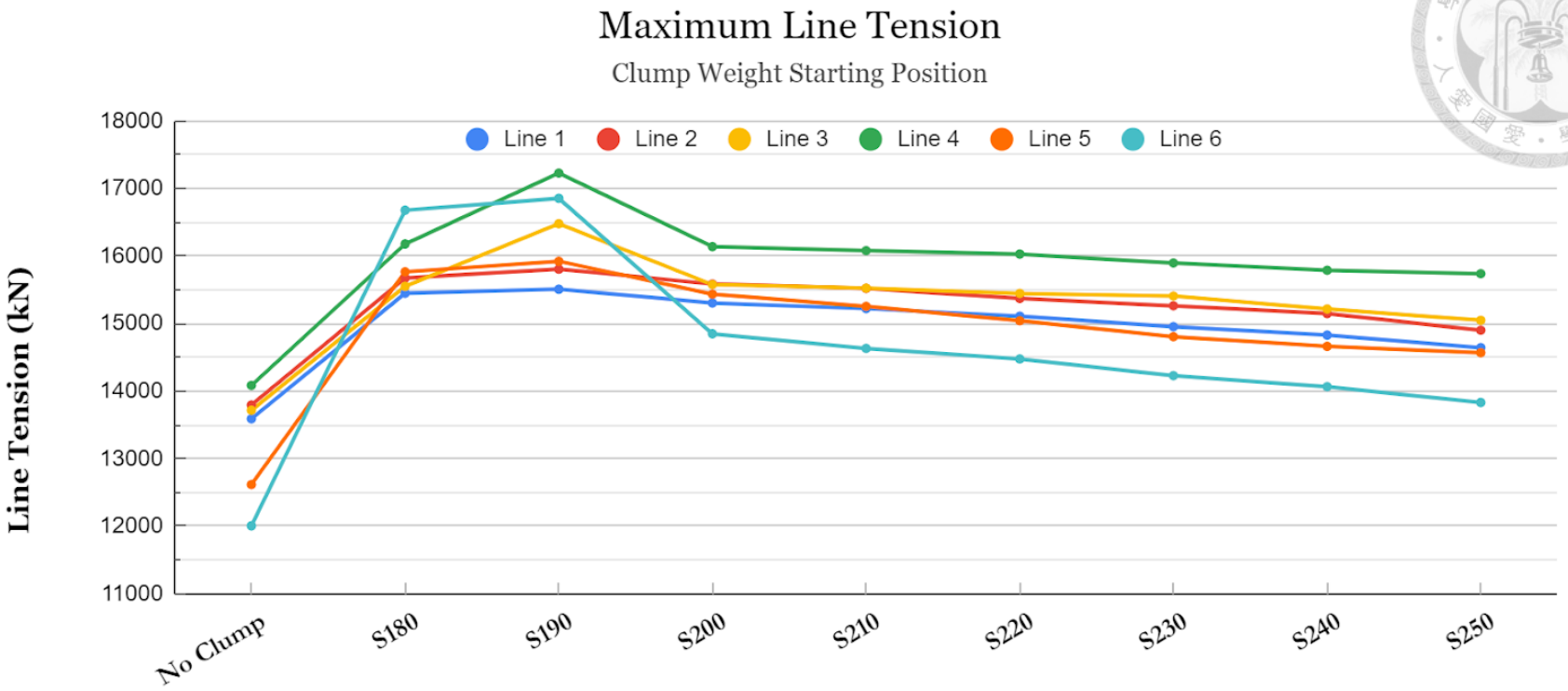

Figure 26. Maximum line tension along mooring lines in control case, S180, S190, S200, S210, S220, S230, S240 and S250

doi:10.6342/NTU202303528

6.2 Clump Weight Spacing

6.2.1 Case Settings

Based on case S250 defined in Section 5.1, the intervals between clump weights vary between 2 m to 7 m. The detail of each case is described in Table 26. The cases labeled as I2, I3, I4, I5, I6, and I7 are specifically designed to examine the impact of clump weight spacing on the mooring system. Each case represents a different spacing configuration ranging from 2 meters to 7 meters. The objective is to assess the effectiveness of varying clump weight spacing in influencing the system's behavior and motion response. Average pretension of mooring lines in each case is shown in Table 27.

Table 26. Cases for study clump weight spacing

Case		No Clump (Control Case)	I2	I3	I4	I5	I6	I7
Starting Position (relative to End connect to TaidaFloat fairlead)		——	250 m					
Clump Weight	Number		13					
	Weight		3 tons					
	Spacing		2 m	3 m	4 m	5 m	6 m	7 m
	Volume		0.5 m^3					

doi:10.6342/NTU202303528

Table 27. Average pretension of mooring lines in control case, I2, I3, I4, I5, I6, I7 and their difference with control case

Case	Pretension (kN)	Difference (%)
No clump	1831.77	0.00
I2	1841.44	0.53
I3	1841.07	0.51
I4	1840.87	0.50
I5	1840.72	0.49
I6	1840.68	0.49
I7	1840.47	0.48

doi:10.6342/NTU202303528

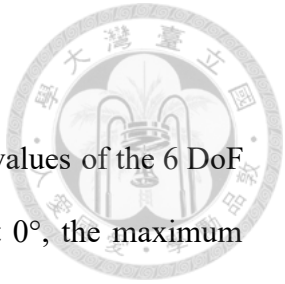

6.2.2 Result and Discussion

Table 28 and Table 34 present the minimum and maximum values of the 6 DoF along with their variances compared to the control model. In I2 at 0°, the maximum surge value reaches 13.00 m, reflecting a 1.00% increase. I2 at 120° exhibits the highest sway value of 13.62 m, showing a difference of 4.87%. For heave, the absolute highest value is 10.27 m, with a difference of 3.12%, also occurring in I2 at 0°. In terms of roll, the maximum value is 10.74°, indicating a significant difference of 21.57% in I2 at 120°. Similarly, for pitch, the maximum value is 13.04°, with a difference of 0.57% observed in case I2 at 180°. Lastly, the maximum yaw value is 14.52°, showing a slight difference of 0.52% in case I2 at 65°.

Table 35 shows that mooring lines maximum tension in case I2 is 57.52% averagely higher than maximum line tension of control case while most maximum tension occurs on the node between the clump weight section. Table 35 and Figure 27 show the maximum line tension occurring at fairlead. The maximum line tension of I2 is higher compared to the control case, with a relative increase of 12.28%, which is not far behind 10.31% for I3, 11.32% for I4, 10.42% for I5, 9.41% for I6, 8.87% for I7. These could be stated as the maximum line tension value depicted in Figure 28. is localized and may not be representative of the entire mooring line.

The maximum line tension occurs in case I2 may be caused by slack snap phenomenon which occurs when a mooring line, which was previously loose or slack, rapidly becomes tensioned or snaps into a tight condition due to external forces or dynamic effects. Additional exploration could be done to determine whether the significant line tension arising within a specific time step has the potential to cause structural damage to the chain. An ideal spacing of clump weights should be designed to distribute the mooring loads evenly across the system.

doi:10.6342/NTU202303528

In summary, it can be concluded that having a relatively small spacing between clump weights can result in localized high line tension. Since the primary effectiveness of the clump weight is desired in the normal sea state, a spacing of 7 meters could lead to the clump weight at the back losing its effectiveness. Therefore, a spacing of 6 meters has been chosen for further study.

Table 28. Minimum and maximum value of surge in control case, I2, I3, I4, I5, I6, I7

	Min			Max		
	Direction (°)	Distance (m)	Difference (%)	Direction (°)	Distance (m)	Difference (%)
No Clump	80	-9.28	0.00	0	12.87	0.00
I2	80	-9.62	3.70	0	13.00	1.00
I3	80	-9.59	3.39	0	12.99	0.95
I4	80	-9.54	2.83	0	12.95	0.62
I5	80	-9.50	2.47	0	12.93	0.47
I6	80	-9.46	2.04	0	12.91	0.34
I7	80	-9.45	1.88	0	12.88	0.12

doi:10.6342/NTU202303528

Table 29. Minimum and maximum value of sway in control case, I2, I3, I4, I5, I6, I7

	Min			Max		
	Direction (°)	Distance (m)	Difference (%)	Direction (°)	Distance (m)	Difference (%)
No Clump	65	-10.65	0.00	120	12.99	0.00
I2	65	-11.03	3.49	120	13.62	4.87
I3	65	-11.04	3.60	120	13.54	4.25
I4	65	-11.02	3.43	120	13.49	3.85
I5	65	-10.99	3.16	120	13.42	3.35
I6	65	-10.96	2.88	120	13.39	3.07
I7	65	-10.94	2.67	120	13.35	2.76

Table 30. Minimum and maximum value of heave in control case, I2, I3, I4, I5, I6, I7

	Min			Max		
	Direction (°)	Distance (m)	Difference (%)	Direction (°)	Distance (m)	Difference (%)
No Clump	0	-9.96	0.00	0	2.51	0.00
I2	0	-10.27	3.12	0	2.45	-2.51
I3	0	-10.23	2.71	0	2.45	-2.69
I4	0	-10.19	2.35	0	2.46	-2.36
I5	0	-10.17	2.09	0	2.46	-2.10
I6	0	-10.15	1.88	0	2.47	-1.86
I7	0	-10.13	1.70	0	2.47	-1.65

doi:10.6342/NTU202303528

Table 31. Minimum and maximum value of roll in control case, I2, I3, I4, I5, I6, I7

	Min			Max		
	Direction (°)	Degree (°)	Difference (%)	Direction (°)	Degree (°)	Difference (%)
No Clump	120	-10.43	0.00	120	8.84	0.00
I2	120	-11.28	8.20	120	10.74	21.57
I3	120	-11.18	7.22	120	10.58	19.72
I4	120	-11.08	6.29	120	10.50	18.81
I5	120	-11.03	5.83	120	10.44	18.11
I6	120	-11.00	5.53	120	10.29	16.39
I7	120	-10.95	4.98	120	10.16	14.94

Table 32. Minimum and maximum value of pitch in control case, I2, I3, I4, I5, I6, I7

	Min			Max		
	Direction (°)	Degree (°)	Difference (%)	Direction (°)	Degree (°)	Difference (%)
No Clump	180	-12.97	0.00	180	4.25	0.00
I2	180	-13.04	0.57	120	5.21	22.75
I3	180	-13.01	0.36	120	5.03	18.31
I4	180	-12.99	0.15	125	4.87	14.64
I5	180	-12.99	0.18	125	4.79	12.73
I6	180	-12.98	0.12	125	4.73	11.41
I7	180	-12.97	0.03	125	4.59	8.13

doi:10.6342/NTU202303528

Table 33. Minimum and maximum value of yaw in control case, I2, I3, I4, I5, I6, I7

	Min			Max		
	Direction (°)	Degree (°)	Difference (%)	Direction (°)	Degree (°)	Difference (%)
No Clump	65	-8.69	0.00	65	14.44	0.00
I2	150	-9.15	5.35	65	14.52	0.52
I3	150	-9.10	4.69	65	14.49	0.30
I4	150	-9.00	3.54	65	14.44	-0.01
I5	150	-8.97	3.27	65	14.42	-0.18
I6	150	-8.87	2.03	65	14.40	-0.27
I7	150	-8.83	1.64	65	14.40	-0.27

doi:10.6342/NTU202303528

Table 34. Maximum line tension along mooring lines in control case, I2, I3, I4, I5, I6, I7

	Line 1		Line 2		Line 3		Line 4		Line 5		Line 6		Average Difference (%)
	Max Tension (kN)	Difference (%)	Max Tension (kN)	Difference (%)	Max Tension (kN)	Difference (%)	Max Tension (kN)	Difference (%)	Max Tension (kN)	Difference (%)	Max Tension (kN)	Difference (%)	
No Clump	13589	0.00	13794	0.00	13716	0.00	14084	0.00	12616	0.00	12004	0.00	0.00
I2	20590	51.52	20368	47.66	21518	56.88	23626	67.75	20678	63.90	18895	57.41	57.52
I3	22858	68.21	21410	55.21	16845	22.81	16204	15.05	22093	75.12	16220	35.12	45.25
I4	14643	7.76	14901	8.03	15048	9.71	15738	11.74	14568	15.47	13831	15.22	11.32
I5	14563	7.17	14883	7.89	14937	8.90	15844	12.50	14203	12.58	13620	13.46	10.42
I6	14489	6.62	14637	6.11	14750	7.54	15435	9.59	14437	14.43	13462	12.15	9.41
I7	14362	5.69	14592	5.79	15062	9.81	15341	8.93	14016	11.10	13435	11.92	8.87

doi:10.6342/NTU202303528

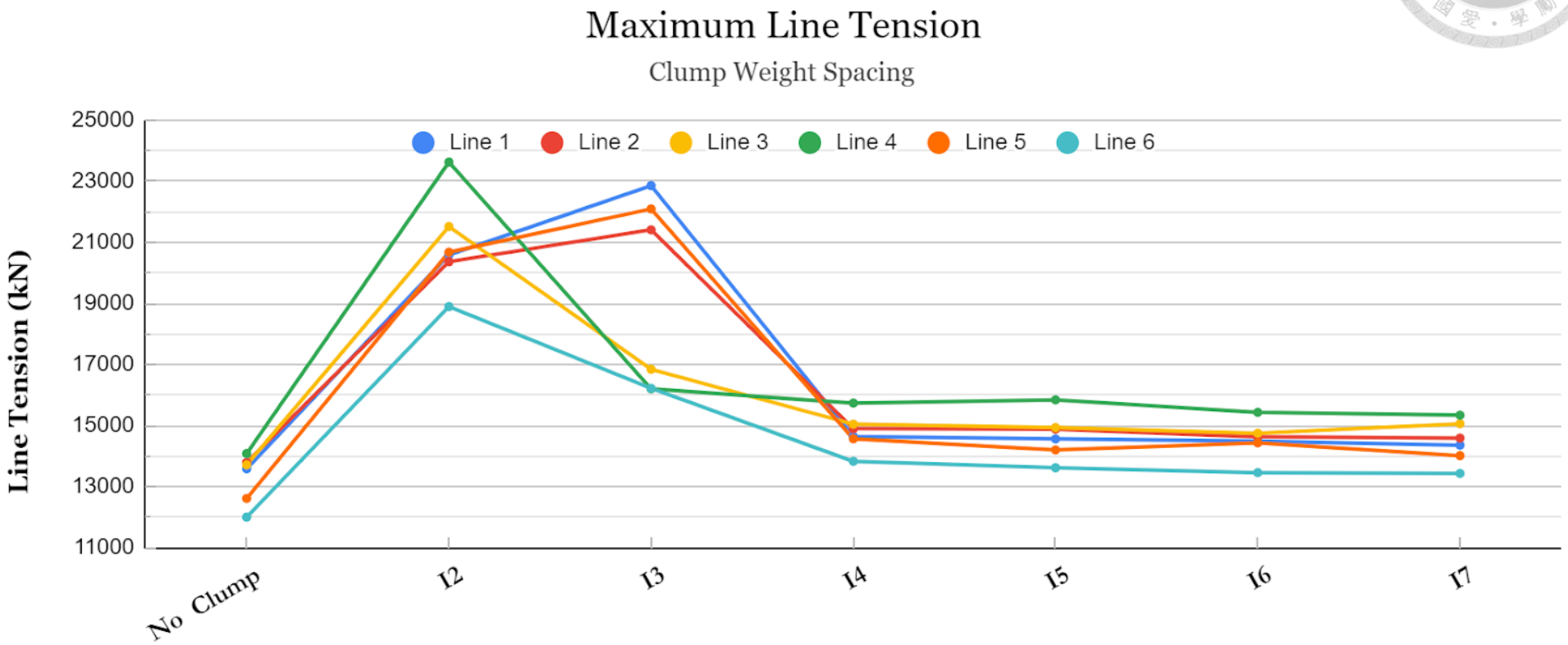

Figure 27. Maximum line tension along mooring lines in control case, I2, I3, I4, I5, I6, I7

doi:10.6342/NTU202303528

Table 35. Maximum line tension at fairlead in control case, I2, I3, I4, I5, I6, I7

	Line 1		Line 2		Line 3		Line 4		Line 5		Line 6		Average Difference (%)
	Max Tension (kN)	Difference (%)	Max Tension (kN)	Difference (%)	Max Tension (kN)	Difference (%)	Max Tension (kN)	Difference (%)	Max Tension (kN)	Difference (%)	Max Tension (kN)	Difference (%)	
No Clump	13589	0.00	13794	0.00	13716	0.00	14084	0.00	12616	0.00	12004	0.00	0.00
I2	13946	2.63	14104	2.25	13979	1.92	14490	2.88	13179	4.46	12556	4.60	3.12
I3	14092	3.70	14278	3.51	14282	4.13	14742	4.67	13482	6.86	12890	7.38	5.04
I4	14213	4.59	14436	4.65	14434	5.23	14993	6.45	13790	9.31	13143	9.49	6.62
I5	14306	5.28	14529	5.33	14607	6.50	15161	7.65	13887	10.07	13361	11.30	7.69
I6	14407	6.02	14644	6.16	14721	7.33	15282	8.51	14014	11.08	13381	11.47	8.43
I7	14489	6.62	14637	6.11	14750	7.54	15435	9.59	14437	14.43	13462	12.15	9.41

doi:10.6342/NTU202303528

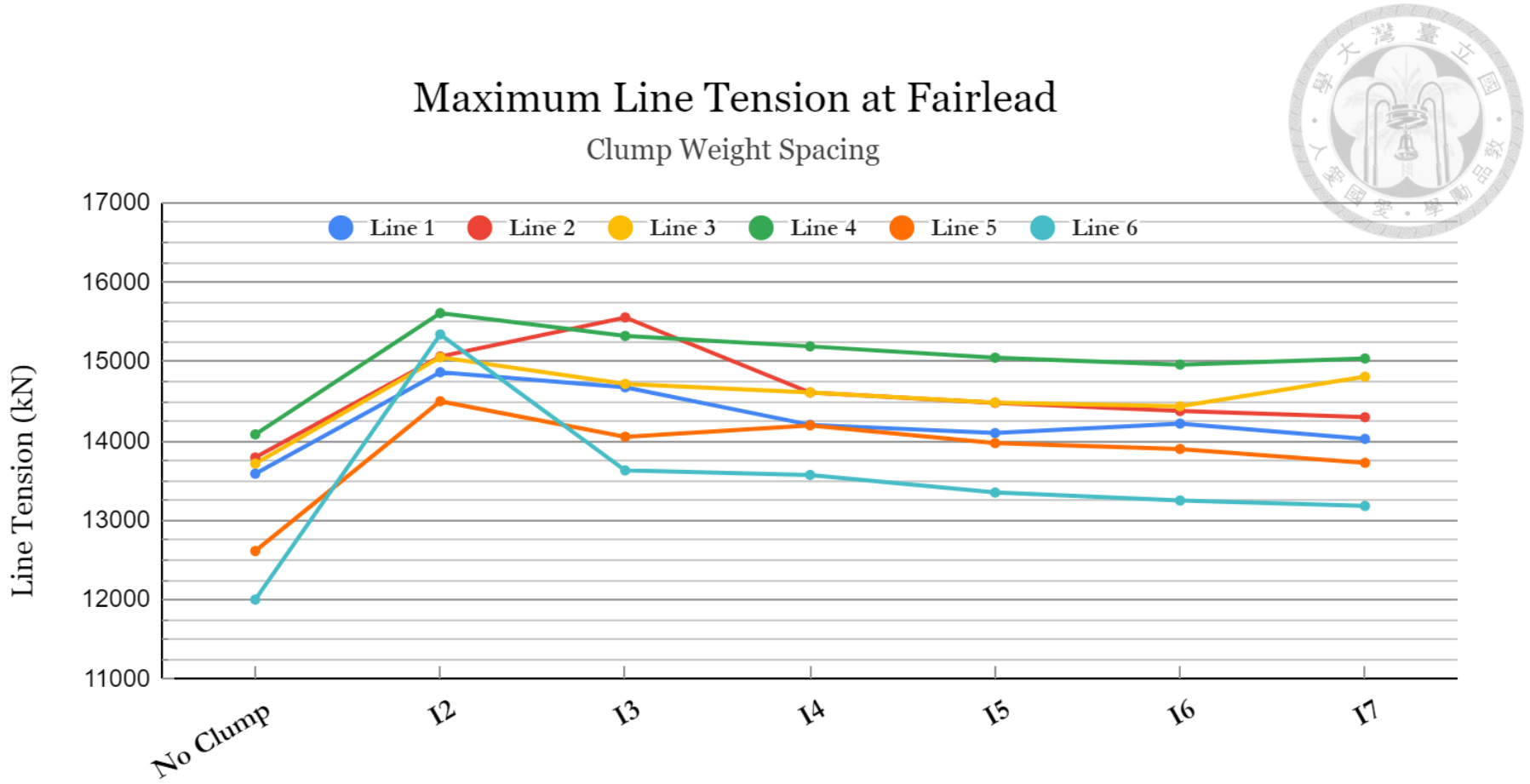

Figure 28. Maximum line tension at fairlead in control case, I2, I3, I4, I5, I6, I7

doi:10.6342/NTU202303528

6.3 Number of Clump Weight

6.3.1 Case Settings

Based on open data for developers, it is evident that the presence installed FOWT of 13 clump weights may be excessive. Therefore, a comprehensive investigation is conducted by examining different numbers of clump weights. Each case involves reducing the number of clump weights by 2 and subsequently performing simulations. A detailed breakdown of each case's specifications can be found in Table 36. The cases labeled as 3C, 5C, 7C, 9C, 11C, and 13C have been specifically designed to explore the influence of the number of clump weights on the mooring system. Each case represents a different configuration, ranging from 3 clumps to 13 clumps. By systematically studying these different parameter settings, valuable insights can be gained regarding the optimal number of clump weights required to achieve the desired performance and stability in the mooring system.

Table 36. Cases for study number of clump weight

Case		No Clump	3 C	5 C	7 C	9 C	11 C	13 C
Starting Position (relative to fairlead)			250 m					
Clump Weight	Number		3	5	7	9	11	13
	Weight	——	3 tons					
	Spacing		6 m					
	Volume		0.5 m^3					

doi:10.6342/NTU202303528

6.3.2 Result and Discussion

Table 37. to Table 42. display the minimum and maximum values for the 6 DoF along with their variances compared to the control model. In Case 7C at 0°, the maximum surge value reaches 12.944 m, representing a 0.59% increase. In Case 13C at 120°, the highest sway value is 13.39 m, indicating a difference of 3.07%. Concerning heave, the absolute highest value is 10.15 m, with a difference of 1.88%, also occurring in Case 13C at 165°. For roll, the maximum value is 11.00°, signifying a notable difference of 5.53% in Case 13C at 120°. Similarly, in terms of pitch, the maximum value is 12.98°, exhibiting a substantial difference of 0.12% observed in Case 13C at 90°. Lastly, the maximum yaw value is 14.53°, showing a slight difference of 0.57% in Case 3C at 65°. Out of the 6 DoF, only the heave motion exhibits a noticeable distinction, and the primary contributing factor may be the difference in weight between the number of clump weights.

Table 43 and Figure 29 display the maximum line tension along mooring lines observed in each scenario, along with the corresponding difference from the control case. The results show that when clump weights position start from arc length 259 m with 6 m of spacing there is no significant difference between cases. FOWT systems consisting of 13 clumps experience the highest line tension, whereas the line tension decreases as the number of clump weights are reduced.

One possible reason for this may be that the touchdown point of the mooring lines is behind the clump weights, causing all of the clump weights to be pulled away from the seabed. The growing line tension is solely attributed to the overall increase in the combined weight of the clump weights. Thus the control case remains the most favorable scenario. The inclusion of clump weights in shallow water should be reconsidered.

doi:10.6342/NTU202303528

Table 37. Minimum and maximum value of surge in control case, 3C, 5C, 7C, 9C, 11C, 13C

	Min			Max		
	Direction (°)	Distance (m)	Difference (%)	Direction (°)	Distance (m)	Difference (%)
No Clump	80	-9.275	0.00	0	12.869	0.00
3 C	80	-9.354	0.85	0	12.926	0.44
5 C	80	-9.399	1.33	0	12.943	0.57
7 C	80	-9.427	1.64	0	12.944	0.59
9 C	80	-9.444	1.82	0	12.935	0.52
11 C	80	-9.457	1.96	0	12.916	0.36
13 C	80	-9.464	2.04	0	12.912	0.34

Table 38. Minimum and maximum value of sway in control case, 3C, 5C, 7C, 9C, 11C, 13C

	Min			Max		
	Direction (°)	Distance (m)	Difference (%)	Direction (°)	Distance (m)	Difference (%)
No Clump	0	-10.65	0.00	120	12.99	0.00
3 C	0	-10.75	0.88	120	13.17	1.39
5 C	0	-10.81	1.46	120	13.25	1.98
7 C	0	-10.86	1.94	120	13.31	2.51
9 C	0	-10.90	2.34	120	13.35	2.81
11 C	0	-10.94	2.69	120	13.37	2.94
13 C	0	-10.96	2.88	120	13.39	3.07

doi:10.6342/NTU202303528

Table 39. Minimum and maximum value of heave in control case, 3C, 5C, 7C, 9C, 11C, 13C

	Min			Max		
	Direction (°)	Distance (m)	Difference (%)	Direction (°)	Distance (m)	Difference (%)
No Clump	85	-9.96	0.00	0	2.51	0.00
3 C	165	-10.04	0.80	0	2.49	-0.97
5 C	165	-10.08	1.25	0	2.48	-1.34
7 C	165	-10.11	1.50	10	2.54	0.97
9 C	165	-10.13	1.72	0	2.47	-1.69
11 C	165	-10.14	1.81	0	2.47	-1.81
13 C	165	-10.15	1.88	0	2.47	-1.86

Table 40. Minimum and maximum value of roll in control case, 3C, 5C, 7C, 9C, 11C, 13C

	Min			Max		
	Direction (°)	Degree (°)	Difference (%)	Direction (°)	Degree (°)	Difference (%)
No Clump	120	-10.43	0.00	180	8.84	0.00
3 C	120	-10.59	1.59	180	9.34	5.66
5 C	120	-10.71	2.70	180	9.59	8.46
7 C	120	-10.79	3.44	180	9.79	10.82
9 C	120	-10.88	4.38	180	10.08	14.08
11 C	120	-10.93	4.84	180	10.17	15.06
13 C	120	-11.00	5.53	180	10.29	16.39

doi:10.6342/NTU202303528

Table 41. Minimum and maximum value of pitch in control case, 3C, 5C, 7C, 9C, 11C, 13C

	Min			Max		
	Direction (°)	Degree (°)	Difference (%)	Direction (°)	Degree (°)	Difference (%)
No Clump	90	-12.97	0.00	180	4.25	0.00
3 C	90	-12.94	-0.21	180	4.23	-0.32
5 C	90	-12.93	-0.24	125	4.33	1.90
7 C	90	-12.94	-0.22	125	4.46	4.94
9 C	90	-12.96	-0.06	125	4.57	7.63
11 C	90	-12.97	0.01	125	4.74	11.63
13 C	90	-12.98	0.12	125	4.73	11.41

Table 42. Minimum and maximum value of yaw in control case, 3C, 5C, 7C, 9C, 11C, 13C

	Min			Max		
	Direction (°)	Degree (°)	Difference (%)	Direction (°)	Degree (°)	Difference (%)
No Clump	0	-8.69	0.00	65	14.44	0.00
3 C	0	-8.69	-0.02	65	14.53	0.57
5 C	0	-8.71	0.30	65	14.49	0.31
7 C	0	-8.77	0.96	65	14.46	0.10
9 C	0	-8.83	1.59	65	14.43	-0.07
11 C	0	-8.86	1.93	65	14.40	-0.27
13 C	0	-8.87	2.03	65	14.40	-0.27

doi:10.6342/NTU202303528

Table 43. Maximum value of line tension along mooring lines in control case, 3C, 5C, 7C, 9C, 11C, 13C

	Line 1		Line 2		Line 3		Line 4		Line 5		Line 6		Average Difference (%)
	Max Tension (kN)	Difference (%)	Max Tension (kN)	Difference (%)	Max Tension (kN)	Difference (%)	Max Tension (kN)	Difference (%)	Max Tension (kN)	Difference (%)	Max Tension (kN)	Difference (%)	
No Clump	13589	0.00	13794	0.00	13716	0.00	14084	0.00	12616	0.00	12004	0.00	0.00
3 C	13946	2.63	14104	2.25	13979	1.92	14490	2.88	13179	4.46	12556	4.60	3.12
5 C	14092	3.70	14278	3.51	14282	4.13	14742	4.67	13482	6.86	12890	7.38	5.04
7 C	14213	4.59	14436	4.65	14434	5.23	14993	6.45	13790	9.31	13143	9.49	6.62
9 C	14306	5.28	14529	5.33	14607	6.50	15161	7.65	13887	10.07	13361	11.30	7.69
11 C	14407	6.02	14644	6.16	14721	7.33	15282	8.51	14014	11.08	13381	11.47	8.43
13 C	14489	6.62	14637	6.11	14750	7.54	15435	9.59	14437	14.43	13462	12.15	9.41

doi:10.6342/NTU202303528

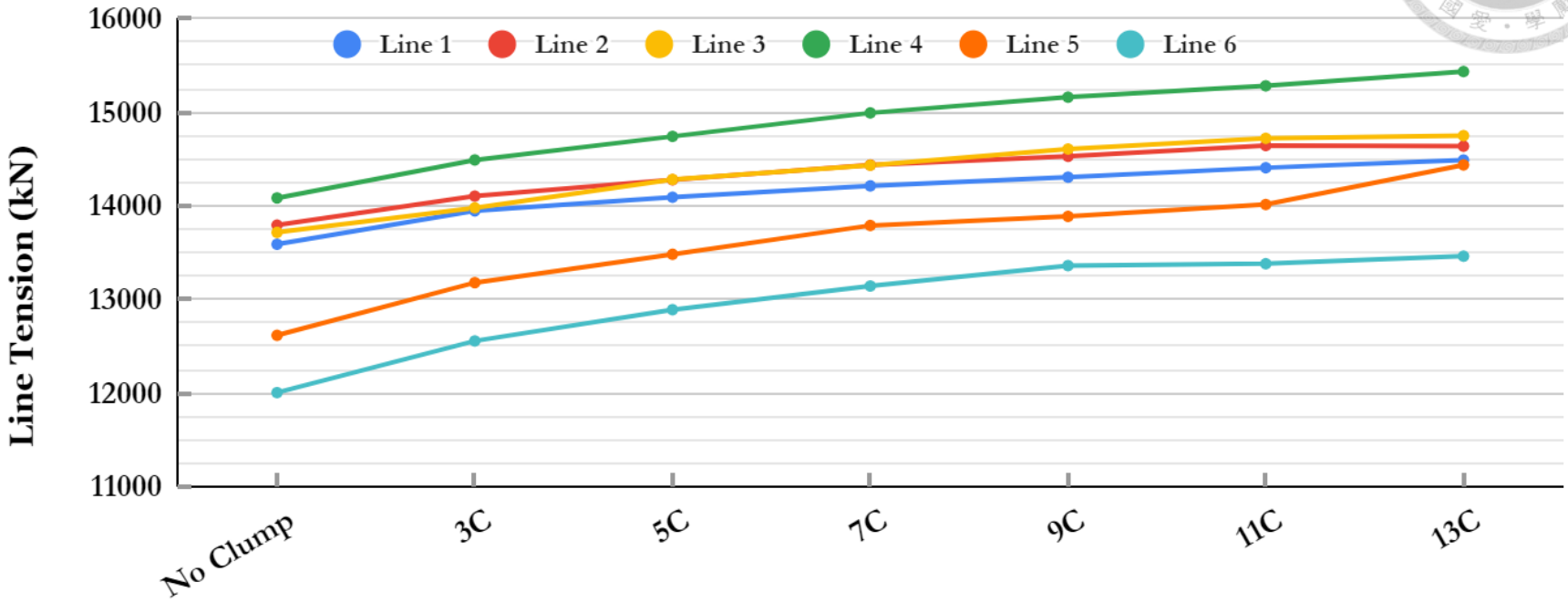

Figure 29. Maximum line tension along mooring lines in control case, 3C, 5C, 7C, 9C, 11C, 13C

doi:10.6342/NTU202303528

Chapter 7

Conclusion

In this study, three parameters related to the clump weight in a mooring system were examined: the initial position of the clump weight, the spacing between clump weights, and the number of clump weights. The investigation focused on extreme sea conditions in shallow water with a 2 MW floating offshore wind turbine (FOWT) system. Based on the findings, the following conclusions could be inferred.

1. Selecting a starting position for the clump weight, which is located after the touchdown point, results in lower line tension and lesser 6 DoF motion.
2. The analysis outputs from Orcaflex suggest that a relatively small spacing between clump weights, in this study, 2 m and 3 m spacing, can result in localized high line tension, which, on average, is 1.5 times higher than the maximum line tension in the control case.
3. The number of clump weights in the range of 3 to 13 does not significantly affect line tension or the 6 DoF motion of the platform. Therefore, there is no benefit to using more clump weights.
4. There is a need to rethink the inclusion of clump weights if the allowable platform offset is generously large (such as 30% water depth assumed for this research work), due to none case with addition of clump weight having better tension compared with control case.

This study suggests that further investigation is needed to explore the feasibility of using clump weights to optimize a FOWT mooring system in shallow water.

doi:10.6342/NTU202303528

References

[1] "Paris Agreement," *Climate Action*. https://climate.ec.europa.eu/eu-action/international-action-climate-change/climate-negotiations/paris-agreement_en (accessed Jun. 30, 2023).

[2] IPCC, *Climate Change 2014: Synthesis Report. Contribution of Working Groups I, II and III to the Fifth Assessment Report of the Intergovernmental Panel on Climate Change*. IPCC, 2014.

[3] P.-C. Chang, R.-Y. Yang, and C.-M. Lai, "Potential of Offshore Wind Energy and Extreme Wind Speed Forecasting on the West Coast of Taiwan," *Energies*, vol. 8, no. 3, pp. 1685–1700, Feb. 2015, doi: 10.3390/en8031685.

[4] H.-F. Fang, "Wind energy potential assessment for the offshore areas of Taiwan west coast and Penghu Archipelago," *Renewable Energy*, vol. 67, pp. 237–241, Jul. 2014, doi: 10.1016/j.renene.2013.11.047.

[5] Executive Yuan, R.O.C. (Taiwan), "Offshore wind-power generation," *Executive Yuan, R.O.C. (Taiwan)*, Dec. 01, 2011. https://english.ey.gov.tw/News3/9E5540D592A5FECD/34ff3d6b-412e-458d-afe9-01737d2da52d (accessed Jun. 30, 2023).

[6] K. M. Wang and Y. J. Cheng, "The Evolution of feed-in tariff policy in Taiwan," *Energy Strategy Reviews*, vol. 1, no. 2, pp. 130–133, Sep. 2012, doi: 10.1016/j.esr.2012.05.002.

[7] Executive Yuan, R.O.C. (Taiwan), "Four-year Wind Power Promotion Plan," *Executive Yuan, R.O.C. (Taiwan)*, Dec. 01, 2011. https://english.ey.gov.tw/News3/9E5540D592A5FECD/d603a1bf-9963-4e53-a92b-e6520a3d93ff (accessed Jun. 30, 2023).

[8] A. M.-Z. Gao, C.-H. Huang, J.-C. Lin, and W.-N. Su, "Review of recent offshore wind power strategy in Taiwan: Onshore wind power comparison," *Energy Strategy Reviews*, vol. 38, p. 100747, Nov. 2021, doi: 10.1016/j.esr.2021.100747.

[9] Y. Chiang, "The Legitimacy and Effectiveness of Local Content Requirements: A Case of the Offshore Wind Power Industry in Taiwan," in *Springer Climate*, Cham: Springer International Publishing, 2023, pp. 119–133. Accessed: Jul. 01, 2023. [Online]. Available: http://dx.doi.org/10.1007/978-3-031-24545-9_8

[10] W.-M. Chen, H. Kim, and H. Yamaguchi, "Renewable energy in eastern Asia:

doi:10.6342/NTU202303528

Renewable energy policy review and comparative SWOT analysis for promoting renewable energy in Japan, South Korea, and Taiwan," *Energy Policy*, vol. 74, pp. 319–329, Nov. 2014, doi: 10.1016/j.enpol.2014.08.019.

[11] H.-S. Chung, "Taiwan's Offshore Wind Energy Policy: From Policy Dilemma to Sustainable Development," *Sustainability*, vol. 13, no. 18, p. 10465, Sep. 2021, doi: 10.3390/su131810465.

[12] Ministry of Economic Affairs,R.O.C., "MOEA Initiates the Offshore Wind Energy Zonal Development Selection Mechanism," *Ministry of Economic Affairs,R.O.C.*, Sep. 12, 2009. https://www.moea.gov.tw/MNS/english/news/News.aspx?kind=6&menu_id=176&news_id=97414 (accessed Jul. 01, 2023).

[13] *Wind Resource Assessment Handbook: Fundamentals for Conducting a Successful Monitoring Program*. 1997.

[14] "Vena Energy to Expand the Development of Offshore Wind Projects in Taiwan," *Vena Energy - Leading Independent Power Producer in the Asia-Pacific region*. https://www.venaenergy.com/news/vena-energy-to-expand-the-development-of-offshore-wind-projects-in-taiwan/ (accessed Jul. 01, 2023).

[15] "CIP 第三階段區塊開發計畫 EN." https://ciptwr3.com/projects.php?lang=en (accessed Jul. 01, 2023).

[16] T. R. Energy, "Taiya Renewable Energy," *台亞風能 Taiya Renewable Energy*. https://www.tre.com.tw/en (accessed Jul. 01, 2023).

[17] N. G. Berg, M. Hess, and S.-E. Jacobsen, "Globa Production Networks and Industrial Restructuring: Unpacking the Emerging Offshore Wind Industry," *Norsk Geografisk Tidsskrift - Norwegian Journal of Geography*, vol. 74, no. 5, pp. 328–329, Jun. 2020, doi: 10.1080/00291951.2020.1776764.

[18] E. I. Konstantinidis and P. N. Botsaris, "Wind turbines: current status, obstacles, trends and technologies," *IOP Conference Series: Materials Science and Engineering*, vol. 161, p. 012079, Nov. 2016, doi: 10.1088/1757-899x/161/1/012079.

[19] "Article Pays Homage to Heronemus and the Enormous Impact of UMass on Wind Energy – UMass Amherst College of Engineering," *UMassAmherst*. https://umass.engineering/historical-collections/homage-heronemus-impact-umass-wind-energy/ (accessed Jul. 01, 2023).

[20] K. Tong and C. Cannell, "Technical and Economical Aspects of a Floating

doi:10.6342/NTU202303528

Offshore Windfarm.," *Wind Engineering*, vol. 17, no. 3, 1993.

[21]N. Barltrop, "Multiple Unit Floating Offshore Wind Farm (MUFOW)," *Wind Engineering*, vol. 17, no. 4, pp. 183–188, 1993.

[22] P. Bertacchi, A. Di Monaco, M. de Gerloni, and G. Ferranti, "A Moored Platform for Wind Turbines," *Wind Engineering*, vol. 18, no. 4, pp. 189–198, 1994.

[23] "DNV-ST-0119 Floating wind turbine structures," *DNV*. https://www.dnv.com/energy/standards-guidelines/dnv-st-0119-floating-wind-turbine-structures.html (accessed Jul. 01, 2023).

[24] K. P. Thiagarajan and H. J. Dagher, "A Review of Floating Platform Concepts for Offshore Wind Energy Generation," *Journal of Offshore Mechanics and Arctic Engineering*, vol. 136, no. 2, Mar. 2014, doi: 10.1115/1.4026607.

[25] S. Butterfield , W. Musial , J. Jonkman, and National Renewable Energy Laboratory , "Engineering Challenges for Floating Offshore Wind Turbines ," in *Copenhagen Offshore Wind Conference* , 2005.

[26] W. Musial, S. Butterfield, and A. Boone, "Feasibility of Floating Platform Systems for Wind Turbines," in *42nd AIAA Aerospace Sciences Meeting and Exhibit*, Jan. 2004. Accessed: Jul. 01, 2023. [Online]. Available: http://dx.doi.org/10.2514/6.2004-1007

[27] S. Bashetty and S. Ozcelik, "Review on Dynamics of Offshore Floating Wind Turbine Platforms," *Energies*, vol. 14, no. 19, p. 6026, Sep. 2021, doi: 10.3390/en14196026.

[28] I.-J. Hsu *et al.*, "Optimization of Semi-Submersible Hull Design for Floating Offshore Wind Turbines," in *Volume 8: Ocean Renewable Energy*, Jun. 2022. Accessed: Jun. 30, 2023. [Online]. Available: http://dx.doi.org/10.1115/omae2022-86751

[29] G. Ferri, E. Marino, N. Bruschi, and C. Borri, "Platform and mooring system optimization of a 10 MW semisubmersible offshore wind turbine," *Renewable Energy*, vol. 182, pp. 1152–1170, Jan. 2022, doi: 10.1016/j.renene.2021.10.060.

[30] D. Timmington and L. Efthimiou, *Mooring Systems for Floating Offshore Wind: Integrity Management Concepts, Risks and Mitigation*. World Forum Offshore Wind e.V., 2022.

[31] K.-T. Ma, Y. Luo, C.-T. T. Kwan, and Y. Wu, *Mooring System Engineering for Offshore Structures*. Gulf Professional Publishing, 2019.

[32] A. Neisi, H. Ghassemi, M. Iranmanesh, and G. He, "Effect of the multi-segment mooring system by buoy and clump weights on the dynamic motions of the floating

doi:10.6342/NTU202303528

platform," *Ocean Engineering*, vol. 260, p. 111990, Sep. 2022, doi: 10.1016/j.oceaneng.2022.111990.

[33] M. J. Harrold, P. R. Thies, D. Newsam, C. B. Ferreira, and L. Johanning, "Large-scale testing of a hydraulic non-linear mooring system for floating offshore wind turbines," *Ocean Engineering*, vol. 206, p. 107386, Jun. 2020, doi: 10.1016/j.oceaneng.2020.107386.

[34] G. Barbanti, E. Marino, and C. Borri, "Mooring System Optimization for a Spar-Buoy Wind Turbine in Rough Wind and Sea Conditions," in *Lecture Notes in Civil Engineering*, Cham: Springer International Publishing, 2019, pp. 87–98. Accessed: Jul. 01, 2023. [Online]. Available: http://dx.doi.org/10.1007/978-3-030-12815-9_7

[35] C.-C. Wu and Y.-H. Kuo, "Typhoons Affecting Taiwan: Current Understanding and Future Challenges," *Bulletin of the American Meteorological Society*, vol. 80, no. 1, pp. 67–80, Jan. 1999, doi: 10.1175/1520-0477(1999)080<0067:tatcua>2.0.co;2.

[36] Bureau of Safety and Environmental Enforcement (BSEE) and Bureau of Ocean Energy Management (BOEM), "Gulf of Mexico Shallow Water Potential Stranded Assets," 2019.

[37] C.-A. Chen, K.-H. Chen, Y. Igarashi, D. Chen, K.-T. Ma, and Z.-Y. Lai, "Design of mooring systen for a 15 MW semi-submersible, TaidaFloat, in Taiwan Strait," in *OMAE2023*, 2023.

[38] N. Bruschi, G. Ferri, E. Marino, and C. Borri, "Influence of Clumps-Weighted Moorings on a Spar Buoy Offshore Wind Turbine," *Energies*, vol. 13, no. 23, p. 6407, Dec. 2020, doi: 10.3390/en13236407.

[39] American Bureau of Shipping, *Guidance Notes on Global Performance Analysis for Floating Offshore Wind Turbines*. 2020. [Online]. Available: https://ww2.eagle.org/content/dam/eagle/rules-and-guides/current/design_and_analysis/206_globalperanalyfowti/fowt-gpa-gn-july20.pdf

[40] American Bureau of Shipping, *Guide for Building and Classing Floating Offshore Wind Turbines*. 2020. [Online]. Available: https://ww2.eagle.org/content/dam/eagle/rules-and-guides/current/offshore/195_fowti/fowt-guide-july20.pdf

[41] INTERNATIONAL ELECTROTECHNICAL COMMISSION, *IEC 61400-1: 2019, Part 3-2: Design requirements for floating offshore wind turbines*. International Electrotechnical Commission, 2019.

[42] Vryhof Anchors B.V. , *Vryhof Manual the guide to anchoring*. 2015. [Online].

doi:10.6342/NTU202303528

Available: https://www.plaisance-pratique.com/IMG/pdf/Vryhof_Anchor_Manual2015.pdf

[43] Orcina, Ltd., "Orcawave Documentation," *Orcina*, 2023. https://www.orcina.com/webhelp/OrcaWave/Default.htm (accessed Jul. 05, 2023).

[44] "OrcaFlex documentation including OrcaFlex API and Python interface," *Orcina*, Jul. 19, 2018. https://www.orcina.com/resources/documentation/ (accessed Jun. 30, 2023).

[45] J. R. Morison and U. of C. Laboratory Berkeley. Fluid Mechanics, *The Force Exerted by Surface Waves on Piles*. 1949.

[46] J. E. W. Wichers, "Slowly oscillating mooring forces in single point mooring systems," in *2nd International Conference on Behaviour of Offshore Structures*, 1979.

[47] 交通部中央氣象局, "天氣 -中央氣象局全球資訊網," 中央氣象局全球資訊網, Jul. 05, 2023. https://www.cwb.gov.tw/V8/C/ (accessed Jul. 05, 2023).

[48] 財團法人船舶暨海洋產業研發中心, *經濟部研究機構能源科技專案 年度執行 報 告 110 年 度 新及再生能源前瞻技術掃描評估及研發推動─ 12mw 級風機抗颱浮式平台與錨繫設計及評估創新前瞻計畫*. 經濟部, 2021.

[49] J. Abild, N. G. Mortensen, and L. Landberg, "Application of the wind atlas method to extreme wind speed data," *Journal of Wind Engineering and Industrial Aerodynamics*, vol. 41, no. 1–3, pp. 473–484, Oct. 1992, doi: 10.1016/0167-6105(92)90451-f.

[50] International Electrotechnical Commission, *Wind energy generation systems - Part 1: Design requirements*. International Electrotechnical Commission, 2019.

[51] W.-H. Yang, R.-Y. Yang, and T.-C. Chang, "Experimental and numerical study of the stability of barge-type floating offshore wind turbine platform," Copernicus GmbH, Mar. 2020. Accessed: Jul. 05, 2023. [Online]. Available: http://dx.doi.org/10.5194/egusphere-egu2020-10179

[52] J. Jonkman, S. Butterfield, W. Musial, and G. Scott, "Definition of a 5-MW Reference Wind Turbine for Offshore System Development," National Renewable Energy Labortary, 2009.

[53] P. ENGINEERING, "Clump weight / sinker - Oval, square & round types," *Pilotfits*. https://pilotfits.com/products/clump-weight-or-sinker/ (accessed Jun. 30, 2023).

doi:10.6342/NTU202303528